UNIVERSIDADE FEDERAL DE MINAS GERAIS
Programa de Pós-Graduação em Engenharia Metalúrgica, Materiais e de Minas

Dissertação de Mestrado

Recuperação de Interfaces Preferenciais em Materiais Monofásicos por Análise de Reflexões Proibidas em Difração de Raios-X Síncrotron

Autor: Lorena Aarão Rodrigues
Orientador: Prof. Dr.-Ing. Augusta Cerceau Isaac Neta
Co-Orientador: Prof. Dr. Angelo Malachias de Souza

Junho/2019

Lorena Aarão Rodrigues

Recuperação de Interfaces Preferenciais em Materiais Monofásicos por Análise de Reflexões Proibidas em Difração de Raios-X Síncrotron

Dissertação de Mestrado apresentada ao Programa de Pós-Graduação em Engenharia Metalúrgica, Materiais e de Minas da Escola de Engenharia da Universidade Federal de Minas Gerais, como requisito para obtenção do Grau de Mestre em Engenharia Metalúrgica, Materiais e de Minas.

Área de Concentração: Metalurgia Física
Orientador: Prof. Dr.-Ing. Augusta Cerceau Isaac Neta
Co-Orientador: Prof. Dr. Angelo Malachias de Souza

Belo Horizonte
Universidade Federal de Minas Gerais
Escola de Engenharia
2019

Rodrigues, Lorena Aarão.
R696r Recuperação de interfaces preferenciais em materiais monofásicos por análise de reflexões proibidas em difração de raios-X síncroton [recurso eletrônico] / Lorena Aarão Rodrigues. – 2019.
1 recurso online (71 f. : il., color.) : pdf.

Orientador: Augusta Cerceau Isaac Neta.
Coorientador: Angelo Malachias de Souza.

Dissertação (mestrado) Universidade Federal de Minas Gerais, Escola de Engenharia.

Apêndices: f. 62-71.

Bibliografia: f. 57-61.
Exigências do sistema: Adobe Acrobat Reader.

1. Engenharia metalúrgica - Teses. 2. Metalurgia física - Teses. 3. Raios X - Difração - Teses. 4. Síncrotron - Teses. 5. Interfaces (Computador) - Teses. I. Isaac Neta, Augusta Cerceau. II. Malachias de Souza, Angelo. III. Universidade Federal de Minas Gerais. Escola de Engenharia. IV. Título.

CDU: 669(043)

Ficha catalográfica: Biblioteca Profº Mário Werneck, Escola de Engenharia da UFMG

To Mai Góthi, Papteks, and Geles.

Acknowledgments

This project was made possible due to the collaboration and encouragement of many people. I am extremely grateful to everyone involved, in one way or another.

To my supervisors, Prof. Dr.-Ing. Augusta Cerceau Isaac Neta and Prof. Dr. Angelo Malachias de Souza - thank you so much for your friendship, patience, trust and good advices. I appreciate the support you have given me for all these years, and for always encouraging me to pursue a better future, academically and professionally.

To professor Roberto Braga Figueiredo for supplying the samples and offering valuable and insightful discussions on the project, and Moara Castro, for all the help during sample preparation and company during the X-ray experiments.

To the XRD1 beamline staff at the Brazilian Synchrotron Light Laboratory (LNLS), for the support during the X-ray diffraction experiments.

To my friends at the Physics and Metallurgical Engineering departments, for the laughs and good times. Special shout-outs to Guilherme, Paula, Hugo, Gisele and the colleagues from the UHV Nanoscopy Laboratory - thank you for sharing the hardships and accomplishments of this journey.

To my family and longtime friends - thank you all so much for the emotional support, motivation and great company. Honorable mentions to the members of Durães Durães: Cecela, Gabrida, Lelê, Gustavo, Yann and Ramon.

To Gabi, my dearest, thank you for the continuous love, patience and support. A lot of the hardships faced during this process were made lighter because you were with me.

Finally, I wish to acknowledge the financial support from agencies CNPq, CAPES, FAPEMIG and CNPEM. Without the funding of these organizations, none of this would be possible.

SUMMARY

List of Figures

List of Tables

RESUMO

O desenvolvimento e o desempenho de materiais metálicos estão intrinsecamente relacionados à nossa capacidade de compreender como tratamentos térmicos, mecânicos e químicos atuam na estrutura até a nano-escala. Nesse sentido, desvendar a estrutura de interfaces destes materiais é crucial para o entendimento de suas propriedades. Os arranjos de interface têm sido caracterizados principalmente por técnicas de imagem, como microscopia eletrônica de varredura e transmissão, que podem acessar dados estruturais localmente, mas são técnicas destrutivas e estatisticamente limitadas. Neste trabalho, um detector de grande faixa angular, cobrindo 120° de ângulo de espalhamento, foi usado para acumular contagens de medições de difração de raios-X síncrotron em amostras de magnésio comercialmente puras. Tempos de aquisição estendidos permitiram a recuperação de configurações de estruturas de interface preferenciais através da observação de picos de difração muito fracos. Picos adicionais foram localizados próximos a reflexões fundamentais do Mg. Uma simulação cinemática de difração de raios-X de interfaces, fazendo uma varredura de estruturas de possíveis para o sistema cristalino em questão, foi realizada para estabelecer a correspondência de picos não-fundamentais com a organização estrutural interfacial de átomos que podem ser responsáveis por tais dispersões. As interfaces simuladas cobriram uma ampla gama de deslocamentos angulares em relação aos principais planos do sistema hexagonal. As informações recuperadas sobre a deformação máxima no plano de interface (em relação a uma configuração bulk) e sua geometria estão relacionadas com condições que levam à minimização de energia local com uma configuração que permite a observação de difração de raios-X, representando um padrão ordenado de distribuições atômicas no Mg. A metodologia introduzida permite o monitoramento não-destrutivo de um sistema cristalino quando este é submetido a processos mecânicos que podem, por exemplo, modificar o tamanho e a orientação de grãos.

Palavras-Chave: *difração de raios-X; síncrotron; interfaces; reflexões proibidas*

ABSTRACT

The development and performance of materials is intrinsically related to our capability of understanding thermal treatments, mechanical processing and chemical alloying down to the nanoscale. In this sense, unraveling the structure of interfaces is crucial for the opening of new regimes in property-performance space for a given material system. Interface arrangements have been mainly characterized by imaging techniques such as scanning and transmission electron microscopy, which can access structural data locally, but are destructive and statistically limited. In this work, a large angular range detector covering up 120° of scattering angle was used to accumulate counts from synchrotron X-ray diffraction measurements on commercially pure Mg samples. Long acquisition times allowed the retrieval of preferential interface structure configurations through the observation of very weak diffraction peaks. Additional peaks were located close to fundamental reflections. A kinematical simulation scanning possible interface structures was carried out to establish the correspondence of non-bulk peaks with the interfacial structural organization of atoms which may be responsible for such scatterings. The simulated interfaces were probed for a wide range of angular displacements with respect to the main cleavage planes of the bulk system. The information retrieved about the maximum strain at the interface plane (with respect to a pure bulk configuration) and their geometry are related with conditions that lead to local energy minimization with a symmetry that allows for the observation of x-ray diffraction, representing a long-range ordered pattern of atomic distributions in Mg. The introduced methodology allows for non-destructive monitoring changes in a system when it undergoes mechanical processes that may, for instance, modify grain sizes and orientation.

Keywords: *x-ray diffraction; synchrotron; interfaces; forbidden reflections*

1. GENERAL INTRODUCTION

Metals and alloys have played fundamental roles in applications and technological developments for several centuries. Despite all progress in improving desirable properties through alloying [1,2], thermomechanical processing [3,4], and the incorporation of reinforcing phases producing metal matrix composites [5], knowledge of the interface structure down to nanoscale is also crucial for designing materials with new regimes of property-performance space [6–8]. The interface structure of polycrystalline metallic materials, such as grain boundaries, subgrain boundaries, twin boundaries, and twist transition boundaries [9–11] strongly influence mechanical [1,12], electronic/optoelectronic [7] and thermal properties. Moreover, interfaces significantly affect diffusion kinetics and consequently mass transport, being thus fundamental to understanding phenomena such as the hydrogen embrittlement [13] and radiation damage evolution [14,15]. Despite the large body of work, there are still important questions on interfaces (or, crystalline defect cores) of metallic systems that remain unanswered, particularly those regarding their atomic arrangements.

The interface structure of metals and alloys has been mainly characterized by imaging techniques such as Scanning and Transmission Electron Microscopy (SEM/TEM), but while SEM and TEM techniques can access structural data locally, they are statistically limited and promote sample degradation. On the other hand, methods that rely on large-area results which are statistically relevant, such as X-ray Diffraction (XRD), may lack of a direct interpretation or depend of specific modeling. For instance, several methods used to determine parameters of the defect structure (e.g., crystallite size distribution, dislocation density, and planar fault probability) consider the breadth and general shape of the diffraction peaks [16].

Recently, the continuous development of third generation synchrotron sources and their associated measurement equipment has opened the possibility of analyzing extremely weak X-ray reflections. These additional intensities are forbidden, non-fundamental reflections that can occur under conditions where the defect lattice has a different periodicity than that of the bulk lattice. With this method, information such as

the interface preferential planes, defect density and formation energies can be extracted. For polycrystalline phases, diffractometer systems equipped with a broad-range detector allow for the simultaneous acquisition of a complete diffractogram with excellent reciprocal space resolution and very large count rate, offering higher accuracy and improved signal-to-noise ratios.

In this work, synchrotron X-ray diffraction experiments were performed in pure magnesium samples using a broad-range detector (Mythen 24K) and long acquisition times, allowing the retrieval of preferential interface structure configurations. A kinematical simulation scanning possible interface structures is required to establish the correspondence between the retrieved non-bulk (forbidden or non-fundamental) peaks with the structural organization of atoms which is responsible for such scatterings. We introduce this methodology by showing how to interpret the datasets in order to reveal the major, most probable interface types. The quantitative advantages over other methods, such as the microscopic specificity of the interface arrangement and the inherently non-destructive X-ray characteristics render such approach unique in the field of Materials Science and Engineering. Through the rotation and matching of parts of the bulk material, it was possible to determine interfacial structures in metals with hexagonal close-packed (*hcp*) crystal structure. Mg and Mg alloys are widely used as a structural material many applications, owing to their high specific strength, low density and stiffness. In addition, the weak scattering of the Mg atoms (low atomic number) makes forbidden peaks hard to detect on weak sources. The method developed here is of general validity with respect to the material choice and can be employed on other polycrystalline and *hcp* metallic systems.

2. BACKGROUND AND APPROACH

2.1. Analysis of X-ray diffraction profiles to determine crystalline defects

Techniques such as transmission electron microscopy (TEM) or electron backscatter diffraction (EBSD) are powerful tools for the characterization of crystalline defects in metals and alloys. However, both TEM and EBSD require cautious and time-consuming sample preparation that will likely impose further deformation and/or degradation of the studied materials.

Meanwhile, X-ray diffraction line profile analysis appeared as a tool that is able to provide statistically relevant information about crystalline defects in deformed metals and alloys. The main goal of this technique is to use the diffractograms as means to determine microstructural parameters such as crystallite size distribution, dislocation density, probability of planar defects, among others. The nature of peak broadening caused by crystallite size, dislocations or planar defects are essentially different, thus allowing the separation of these effects and the determination of their characteristic parameters [16].

Several methods were developed to extract the microstructural parameters from the reflections whose structure factor for the bulk is not zero (fundamental reflections). Initially, peak width was used to determine the average size of crystallites and microdeformation of the crystal lattice. Within this category, the classic method of Williamson-Hall (1953) is the most employed. Later, this procedure was improved by Ungár and Borbély (1996) so that the peak broadening caused by anisotropic deformations was considered. In this context, anisotropic deformation means that the deformation component on the broadening of peaks is strongly dependent of the Miller indexes (hkl). A similar modification was made in another important method known as the Warren-Averbach analysis (1990), which was able to provide characteristic parameters of the dislocation structure and the probability of planar defects, as well as crystallite sizes, in a work developed by Ungár et al. (1998). These methods require the evaluation of several reflections in order to obtain a successful analysis.

Unlike the methods quoted above, some methods are based on the study of a single reflection. One of them is known as the Variance Method, which highlights the models developed by Wilson (1955) and Groma (1998). This method uses the normalized decay of the Bragg peak intensities to determine crystallite sizes and the characteristics of dislocation structures. Another equally in-depth method proposed by Capello et al. (2005) [17] is based on the analysis of the power law governing the intensity decay of the diffraction peaks and its asymmetry (known as *Huang scattering*) in the reciprocal space. This allows the extraction of elastic deformation values from the crystal lattice existing around the defect, and its dimensionality (punctual, linear, or planar).

Finally, with the increase of computational capacity, methodologies were developed for the analysis of X-ray diffraction profiles based on techniques of adjustment of the whole diffraction pattern. There are several profile fitting software to evaluate the diffractograms of polycrystalline materials, such as MAUD, FULLPROF, FOX, MStruct, MWP, WPPF, WPPM and CMWP [16]. All profile analysis methods for the characterization of defects in polycrystalline materials are based on indications present on Bragg peaks for fundamental reflections.

With the advent of synchrotron light sources, it's possible to obtain complete diffractograms with a much superior intensity than those measured in conventional equipments due to a combination of high brightness of the source and the use of high-count, large area detectors. As an example, the XRD1 beamline of the Brazilian Synchrotron Light Laboratory (LNLS) [18] offers a solid-state detector (Mythen 24K) covering up 120° of scattering angle, in addition to the dipole accelerator on the source of the synchrotron beam. That can be used to accumulate counts from synchrotron XRD with a large gain when compared to conventional XRD equipment. In such conditions, the count rate increases over a factor of 10^8 with respect to a conventional lab equipment due to the photon flux of the source, considering approximately 10^{11} photons/s at the sample position in the synchrotron source and 10^7 photons/s in a standard laboratory source. Another 10^4 factor is introduced due to the large-range detector, which measures 30720 points and is used over 1 hour accumulation (in the present study). If such diffractogram would be made point by point with 1 sec accumulation per point, it would require 8 hours to complete a measurement. Hence, acquiring 1h data in a long-arc system

such as the one described above improves the signal-to-noise ratio by an additional factor of 10^5. With such enhancements, the observation of very weak diffraction peaks becomes feasible. One can then retrieve information about weak scatterers such as segregated impurities or non-bulk structures that have reduced total volume (e.g. interfaces or other defect structures) inside the polycrystalline matrix.

In recent times, Nordlund (2002) introduced a fully atomistic modeling scheme to calculate and predict the diffuse X-ray scattering patterns from 311 defects in Si through reciprocal space maps [19]. The results, later confirmed by experimental data [20], demonstrated how both the defect width and length can be derived from the scattering intensities; most importantly, it demonstrated that X-ray methods can be used as a nondestructive, statistically relevant rapid method to characterize defects when combined with computer simulation predictions. More recently, Oliveira et al. (2014) [21] have shown that the use of reciprocal space maps and HRTEM simulations associated with synchrotron X-ray diffraction data could reveal additional intensities (reflections) which arise from crystalline defects in deformed thin CdTe films (*Figure 2.1*). Analysis of the maps allowed the retrieval of the lattice strain due to the presence of double-twin interfaces, as well as the evaluation of average defect size and density. These additional intensities are "forbidden reflections" for the bulk material, but occur under conditions where the atomic structure of the interfaces have a different periodicity than that of the original lattice (thus diffracting under permitted Bragg conditions for its arrangement).

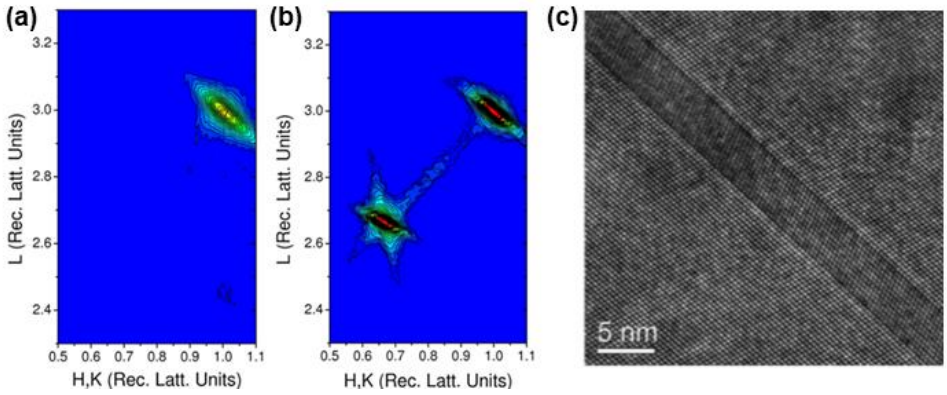

Figure 2.1 - Reciprocal space maps of a CdTe sample in the vicinity of (113) reflection: **(a)** (113) reflection without defect-induced intensities **(b)** (113) reflection with an additional reflection induced by double-twinning of the sample after plastic deformation. **(c)** HRTEM image of the defect. (Oliveira et al., 2014).

2.2. Severe Plastic Deformation

The induction of severe plastic deformation in metallic materials is a mean to increase resistance of metals and alloys through grain refinement, and it can depend on factors like temperature, strain rate and strain direction. Metalworking processing can affect material microstructure in different ways; the techniques used in this work are hot-rolling and Severe Plastic Deformation (SPD). Equal Channel Angular Pressing (ECAP) is one of the most common SPD techniques used for the synthesis of bulk ultrafine-grained or nanostructured materials, which can usually provide significant improvements on mechanical properties [22]. ECAP consists of the extrusion of a sample through a corner matrix (*Figure 2.2*), where the imposed strain is dependent on temperature, corner angle and number of passes through the channel. This processing can be repeated indefinitely as it promotes deformation without changing sample cross-section, leading to progressive amounts of deformation and structure refinement [23]. Since many of the fundamental properties of crystalline materials are dependent on grain size, SPD processing emerges as a powerful tool for producing materials with interesting properties, such as high strength or superplasticity [24].

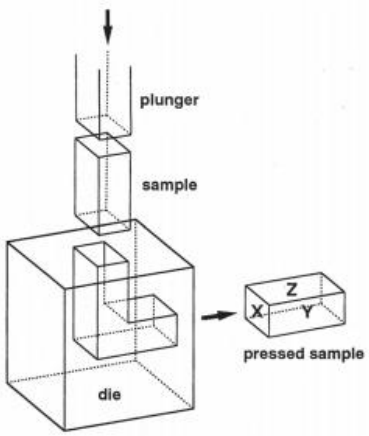

Figure 2.2 - Equal Channel Angular Pressing scheme. (Nakashima et al., 2000).

When dealing with hexagonal close-packed materials, the grain refinement during SPD processing has different features than in other materials. For instance, there is evidence in Mg alloys that, above a critical initial coarse grain (CG) size, the grain refinement starts with the development of an inhomogeneous grain structure, with the new grains forming along the boundaries of the initial coarse grains (*Figure 2.3*). With

increasing strain, the grain refinement then spreads into the initial grain interiors, thereby leading to a more homogeneous fine grain structure. In *hcp* metals and alloys, dislocation mechanism of grain refinement requires the activation of both non-basal and basal slips [25], with dislocations on the basal plane having their activation made easier by external stresses. The glide on non-basal slip systems is more difficult, but the activation of these dislocations is facilitated by applying high stresses or elevated temperatures. Therefore, the stress concentrations induced by SPD at the boundaries of the initial grains yield the activation of both basal and non-basal slip processes, leading to the formation of fine grains at the pre-existing grain boundaries [26].

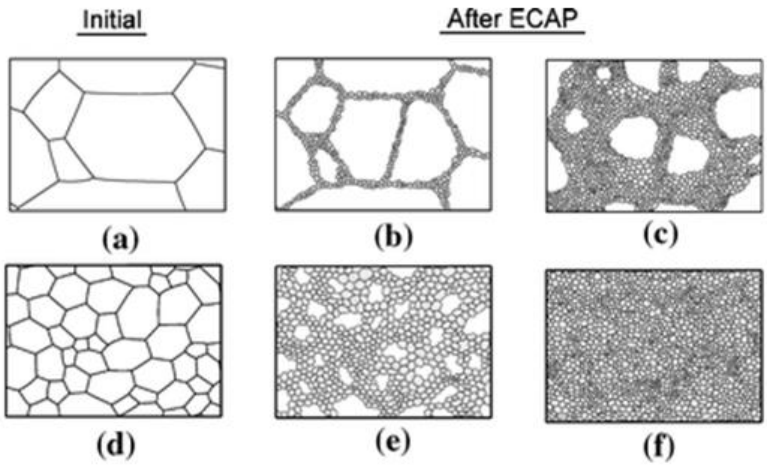

Figure 2.3 - Model for grain refinement of Mg after progressive passes of ECAP. Different initial grain structures like **(a)** and **(d)** can lead to distinct refinement mechanisms. [27]

2.3. Interface structure in ultrafine-grained materials

Surfaces and interfaces play a particularly critical role in determining the mechanical behavior of materials that undergo different processing techniques. The concept of a hierarchical structure can be implemented to analyze the behavior of a material containing multiple length scale structures, either by being a single-phase material with inhomogeneous microstructure or by being a composite material [11]. The implementation of this concept enables the analysis to isolate the strengthening contributions of the various components within the hierarchical structure. The hierarchical interface structures in ultrafine-grained (UFG) materials can be characterized

under the following scheme: Level (0), consisting of boundaries between CG and UFG; Level (1), CG/CG and UFG/UFG boundaries; and Level (2), subgrain boundaries, twin structures and other special interfaces/boundaries. With this work being a statistical analysis of the presence of defects in mechanically deformed materials, a correlation that pinpoints exactly the contributions of each hierarchy levels may not be readily made.

In *hcp* systems in general, the dominant deformation mode and main strengthening mechanism in addition to slip is known as *deformation twinning*. The appearance of twins is a phenomenon of great importance in hexagonal close-packed (*hcp*) materials like magnesium, titanium, and zirconium - the *hcp* structure is the most likely to form deformation twins when strained due to its limited number of available slip systems. In particular, studies on magnesium and its alloys show correlations between the initial microstructure and the formation of twin defects [28], and suggest that the induction of these defects by deformation processes can influence grain size and dislocation density, and also contributes to improve resistance. There are also suggested connections between twinning and anisotropic mechanical behavior of Mg-based materials. Additionally, stress vs. strain curves can indirectly indicate the formation of twin defects [26–28]. Twinning on the $\{10\bar{1}2\}$ plane is the most common plastic deformation mode for hcp [29,30], although there have been reports on other twinning planes and other unusual configurations [12].

Despite that, previous studies also show that the probability of twinning happening in *hcp* structures decreases with decreasing grain size [33], which can be explained by the stress dependence of deformation mechanisms. The strain along the basal plane results from the easy glide of dislocations with <*a*>-type Burgers vectors. At the same time, the deformation in the direction of the crystallographic *c*-axis may be performed by glide of dislocations with <*c*+*a*>-type Burgers vectors or by twinning, since both processes operate mainly on pyramidal planes. An elevated deformation temperature and/or high stresses can increase the activation of pyramidal <*c*+*a*> dislocations at the expense of twin formation. In deformed *hcp* metals with smaller grain size, the stresses are higher mainly in the vicinity of grain boundaries [26], which facilitate the operation of dislocations, thereby reducing the occurrence of twinning.

In addition to the already documented XRD line profile analysis techniques [34], the use of transmission electron microscopy (TEM) or electron backscatter diffraction (EBSD) techniques in materials that have been subjected to such deformation processes allows visualization and verification of the most common induced defects and their microstructure, texture evolution and occurrence of specific types of defects [35]. Theoretical calculations and TEM observations for *hcp* metallic materials suggest the activation of <*c*+*a*> dislocations by strong deformation at elevated temperatures [36]. At room temperature, the critical resolved shear stress of pyramidal <*c*+*a*> dislocations is larger than the basal slip [37], and tends to decrease with higher temperatures.

For *hcp* crystals, most atomistic simulation studies involving topological models, density functional theory (DFT) or molecular dynamics (MD) have been used to determine the atomic structure of grain boundaries with minimum energy, focusing mostly on coherent, symmetric tilt grain boundaries (STGBs). Structure predictions of common, uncommon and previously unobserved coherent twin boundaries have been modeled [38], but interfaces that deviate from exact coincidence may still have a multiplicity of atomic structures that compose them. That highlights the importance of evaluating both geometric and energetic aspects when searching for preferential structure configurations in computational simulations, since minimum-energy configurations can also be manifested through asymmetric boundaries (*Figure 2.4*) [39].

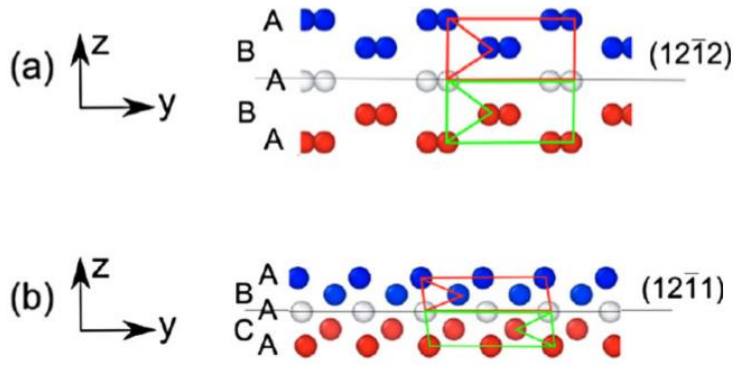

Figure 2.4 - Example of **(a)** symmetric and **(b)** asymmetric configurations of Mg interfaces with low energies. [39]

2.4. Fundamentals of X-ray Diffraction

The phenomenon of X-ray diffraction consists basically on the scattering and interference effects that an incident X-ray beam undergoes when interacting with a material. The study of this effect allows for the determination of the atomic and molecular structure of the samples, phase identification, information on the size distribution of grains in a polycrystalline sample, orientation (texture), among others. In a crystalline material where atoms are organized periodically in planes with characteristic spacing, the classic treatment of coherent (elastic) scattering is the main process investigated.

In elementary treatments of X-ray scattering, diffraction occurs according to Bragg's law:

$$n \cdot \lambda = 2 \cdot d_{hkl} \cdot \sin\theta \tag{2.1}$$

This is the condition to be satisfied for the constructive interference of waves with an angle of incidence θ, for a set of crystallographic planes (hkl) separated by an interplanar distance d_{hkl} (*Figure 2.5*). The diffracted beam is essentially composed of scattered rays where path differences will arise naturally, seeing that a crystalline material is a repetition system; fulfillment of Bragg's law will, therefore, follow the conditions:

- On a few directions which satisfy Bragg's law, the scattering X-ray amplitudes add up and form diffractions peaks or spots (constructive interference);
- On most other directions, which do not satisfy Bragg's law, the scattering X-ray amplitudes cancel each other out, forming no diffraction peaks or spots (destructive interference).

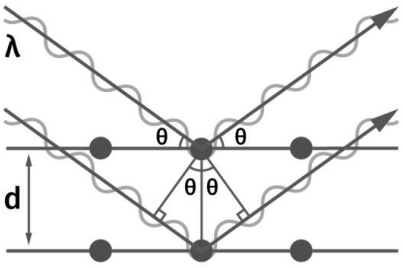

Figure 2.5 - Schematic representation of Bragg's law (adapted from Stresstech Ltd.).

It's important to note that fulfillment of Bragg's law, and consequently diffraction, can occur by varying of any terms in the equation; therefore, the preferred mode for its application will depend on what factors one would want to obtain or study in the configuration of interest.

The method of interest in the present work is the *powder diffraction* method, where wavelength (beam energy) is kept fixed while the angle is varied. This is an ideal method to study materials with randomly oriented microcrystals in relation to the incident beam (powder materials, polycrystalline samples, and others). For those types of samples, the random orientation of the microcrystals relative to the incident beam is such that a statistically significant number of any set of planes will have a chance to diffract the X-rays - that is, will be in the proper orientation to satisfy Bragg's condition - and manifest itself in the diffraction pattern. That is the equivalent of focusing the beam on a crystalline material rotated through all possible angles. Therefore, any diffraction pattern collected over powder method will be composed of multiple Bragg peaks obtained in different conditions, which in turn will each have different intensities, shapes and different angular positions. Furthermore, the use of a synchrotron X-ray radiation source for powder diffraction experiments has several advantages: since the high intensity and collimation of the beam provide a better spatial resolution of the incident/diffracted X-rays, we consequently have an improvement in angular resolution, useful for indexing unknown peaks. Other factors include a better signal-to-noise ratio and possibility to use different wavelengths (energies) from a continuous spectrum, among others.

2.3.1. *Kinematic Scattering Formalism*

In general, the interaction of a crystalline material with X-rays is a complex process [40]. There are two levels of approximation for the treatment of this kind of interaction: the *kinematic* and *dynamic* scattering formalisms (approximations). The main difference between the two is related to the possibility (or not) that the scattered beam can be scattered multiple times before leaving the crystal: on the *kinematic diffraction*, an X-ray beam is not scattered more than once, and therefore it's considered that interactions

between the material and the diffracted beam are weak. For this to be accomplished, it is then postulated that:

1. a crystal consists of individual crystallites slightly misaligned with each other;
2. crystallite size is small enough (microcrystals);
3. the misalignment between crystallites is large enough so that the interaction of X-rays with the material beyond the size of the crystallites is negligible.

The formalism of *dynamic diffraction*, on the other hand, takes into account other types of wave interaction beyond scattering of the incident wave, and its required only when dynamic effects become significant, as is the case of near-perfect crystals. Since these effects are not observable for the majority of crystalline materials, the use of kinematical approximation is more adequate and simpler, especially in the analysis of polycrystalline materials (crystallites of reduced size). For that reason, the present study will limit itself to the use of kinematical formalism.

2.3.2. *Structure Factor for a Bragg Reflection*

The integrated intensity of a Bragg peak is primarily a function of the atomic structure of the crystalline material, but is also dependent on secondary factors such as sample parameters (like grain size and distribution) and instrumental parameters. Structural parameters are, in general, the ones with greater influence on the integrated intensity, and will be the main focus of study in this work.

Elastic scattering must be considered for all the atoms that make up the crystal so that we can arrive at an expression for the scattered amplitude of the diffracted beam. Assuming that Bragg's law is satisfied, the scattered amplitude will basically be a function of atomic coordinates: if a crystal is nothing more than a repetition system of a fundamental unit cell (among the 14 known Bravais lattices), it suffices to consider how the atomic arrangement of just a single unit cell affects the scattering amplitude of a diffracted beam. The sum of this amplitude over the whole repetition system will give us the scattered amplitude of the whole crystal.

In a simplified way, the structure factor $|F_{hkl}|^2$ is given as the square of the absolute value the of scattering amplitude (diffracted intensity) on a crystalline material. According to the kinematic scattering approximation, this amplitude is treated as a sum over all atoms in the unit cell:

$$\mathrm{F}_{hkl} = \left|\sum_{\mathrm{i}} f_{\mathrm{i}}\, \mathrm{e}^{\sigma} \mathrm{e}^{2\pi i\, \vec{\mathrm{R}}}\right|^2 = \left|\sum_{\mathrm{i}} f_{\mathrm{i}}\, \mathrm{e}^{\sigma} \mathrm{e}^{2\pi i\, (hx+ky+lz)}\right|^2 \tag{2.2}$$

In addition to the atomic positions within the unit cell defined by the vector $\vec{R} = hx + ky + lz$, for a (hkl) reflection that satisfies Bragg's law, the structure factor also suffers contributions from other structural factors: term f_i represents the *atomic scattering factor* (a multiplier function dependent on the electronic distribution of each element present in the unit cell), and σ represents the *Debye-Waller factor* (a thermal motion attenuation function).

For a hexagonal close-packed lattice, which is the structure of the studied material in this work, we have base vectors whose in-plane lattice parameters a and b in the unit cell are equal and positioned at a 120° angle, and an out-of-plane lattice parameter c such that $a = b \neq c$ and $\alpha = \beta = 90°, \gamma = 120°$ (*Figure 2.6*). From Bragg's law, its interplanar distance is given by [41]:

$$\frac{1}{\mathrm{d_{hkl}}^2} = \frac{4}{3}\left(\frac{h^2+hk+k^2}{\mathrm{a}^2}\right) + \frac{l^2}{\mathrm{c}^2} \tag{2.3}$$

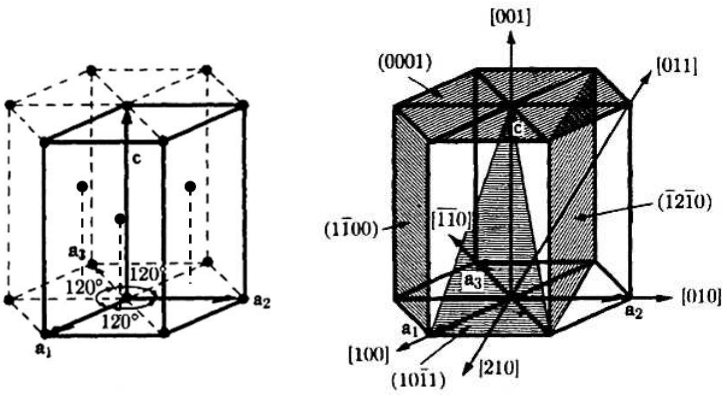

Figure 2.6 - Schematic representation of the *hcp* crystal lattice and its main planes and directions (Cullity, B. D. 2001).

In this case, we have a unit cell composed of only two atoms, located at positions 0 0 0 and $\frac{1}{3}\frac{2}{3}\frac{1}{2}$; its structure factor/wave amplitude (considering only the atomic positioning) is going to be expressed as:

$$\mathrm{F}_{hkl} = f\mathrm{e}^{2\pi\mathrm{i}(\mathrm{h}\cdot 0+\mathrm{k}\cdot 0+\mathrm{l}\cdot 0)} + f\mathrm{e}^{2\pi\mathrm{i}(\mathrm{h}/3+2\mathrm{k}/3+\mathrm{l}/2)}$$

$$= f\left[1 + \mathrm{e}^{2\pi\mathrm{i}\{[(\mathrm{h}+2\mathrm{k})/3]+\mathrm{l}/2\}}\right]. \tag{2.4}$$

Since this expression can be either real or complex, multiplication by the complex conjugate will give the square of its absolute value - $\mathrm{F}_{hkl}^2 = \mathrm{F}_{hkl}\mathrm{F}_{hkl}^*$:

$$|\mathrm{F}_{hkl}|^2 = f^2\left[1 + \mathrm{e}^{2\pi i[(h+2k)/3+l/2]}\right]\left[1 + \mathrm{e}^{-2\pi i[(h+2k)/3+l/2]}\right]$$

$$= 4f^2\cos^2\pi\left(\frac{h+2k}{3} + \frac{l}{2}\right). \tag{2.5}$$

Observing the conditions of the Miller indexes h, k and l in which the exponential factor takes an integer value, we'll then have that the structure factor for the *hcp* structure can assume four forms:

$$\begin{cases} h+2k = 3n\,, l = even: & F_{hkl}^2 = 4f^2, \\ h+2k = 3n \pm 1\,, l = odd: & F_{hkl}^2 = 3f^2, \\ h+2k = 3n \pm 1\,, l = even: & F_{hkl}^2 = f^2, \\ h+2k = 3n\,, l = odd: & F_{hkl}^2 = 0. \end{cases} \tag{2.6}$$

It is noted that the last condition has a structure factor equal to zero, so any set of planes that meet this condition in a bulk system will *not* appear in the diffraction pattern since these reflection's intensity will be cancelled out (destructive interference). These conditions can be important to verify the occurrence of forbidden reflections (zero intensity) and investigate the appearance of additional reflections as a direct result of crystalline defects (induced or not).

It's also noteworthy that, for its simplicity, the formalism presented to obtain the structure factor and the diffracted intensity in a crystal can be reproduced in computational simulations applied to different systems, having defined the configurations to be investigated along with their appropriate lattice symmetry.

The main focus of this work is to study the manifestation of grain boundaries and/or inner-grain defects (interfaces) in a single-phase polycrystalline metal, which in this case is commercially pure magnesium (CP-Mg). As presented before, a portion of these defect configurations can be categorized under *twinning* (symmetric defect where the junction between two crystals can be characterized as a "reflection" along a common plane, axis or point); in such cases, the atomic configuration on the interface plane of a twin-like defect of an *hcp* system is characterized by a face-centered cubic (*fcc*) structure. *Figure 2.7* represents the most common slip and twinning planes for the hexagonal close-packed crystal structure. Despite these planes being the most commonly observed for this system, all configurations in between could also manifest themselves in a real sample (processed or not), with more or less probability depending on energy minimization conditions. Therefore, the investigation of *all* possible planes inside the *hcp* lattice, passing through the most commonly observed ones, could be of interest.

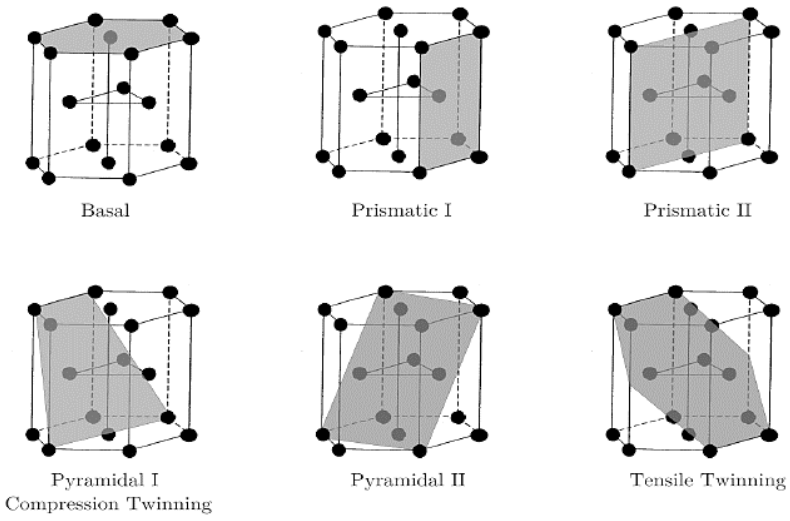

Figure 2.7 – Common slip and twinning planes of the HCP system (Jaber, 2015).

2.4. Objectives and Outline of the Dissertation

This work presents a novel approach for providing statistically relevant information on the atomic arrangement of interfaces in *hcp* materials (here, singe-phase commercially pure Mg) subjected to deformation and refinement processing. A better comprehension of the interface structure down to nanoscale is crucial for understanding the relation between microstructure and mechanical properties, and designing materials with new regimes of property-performance space.

To achieve that, synchrotron X-ray diffraction of the samples were performed with long acquisition times using a large-area reciprocal space detector, thus allowing the retrieval of forbidden (non-fundamental) reflections that indicate the existence of preferentially oriented interfaces. The Mg samples were evaluated in three distinct conditions: (i) processed by hot-rolling, (ii) processed by hot-rolling followed by tensile test, and (iii) processed by hot-rolling and SPD (ECAP) followed by tensile test. The combined rolling and ECAP processing were used to obtain grain refinement (i.e., high density of interfaces) with a homogeneous microstructure; the samples were further subjected to tensile tests in order to promote the generation of new crystalline defects for accommodating the plastic deformation and, consequently, higher density of interfaces. Kinematical simulations scanning possible interface structures were then performed to establish the correspondence of the forbidden peaks with the interfacial structural organization of atoms that were responsible for such scatterings. We conceptualize the simulation routines to reproduce the crystalline structure at the most basic level (a crystal with no defects) and verify its effectiveness and compatibility with a bulk XRD profile. After the routine is optimized, we take on the most important step, which is the attempt to reproduce the experimental profiles through the scanning of different arrangements of interfaces (rotation and matching of bulk crystals), determining the most probable interfacial configurations.

Concerning the outline of this dissertation, Chapter 3 presents the Materials and Methods section with an overview of the studied samples, XRD experiments and simulations. The Results and Discussion sections are presented in Chapters 4 and 5, respectively. Finally, Chapter 6 summarizes the conclusions of this work.

3. MATERIALS AND METHODS

3.1. Materials

The samples studied in this work consist of commercially-pure magnesium (99.9%). The material was provided by Rima Industrial S/A (Várzea da Palma, Brazil) as as-cast slabs with about 10 mm thickness. Samples were cut from the as-cast slabs and rolled to a thickness of 1 mm at a temperature of 673 K. Rectangular plates with 60 × 9.4 × 1.0 mm were extracted from the rolled sheets. The plates were piled in groups of nine and covered with a copper sheet of 0.3 mm thickness to obtain a prismatic bar with 60 × 9.4 × 9 mm which was processed by 4 passes of ECAP at 473 K using route C (sample is rotated 180° between each pass). Tensile specimens were machined from samples subjected to both rolling and ECAP processing. Testing was carried out in an Instron machine model 5582, at constant rate of crosshead displacement. Details of these procedure can be found in [27]. Finally, optical metallography of the samples was carried in a conventional optical microscope to evaluate the microstructure. The sample preparation consisted of grounding in abrasive papers, polishing, and chemical etching with a solution of 5% nitric acid in ethanol to reveal grain structure.

Table I below contains the received sample listings and specifications regarding their deformation tests:

Table I - Listing of the CP-Mg slab samples. *****Samples *T1, T2* and *T5* were the ones chosen to do direct comparisons with the subsequent simulations.

	Designation	Tensile Test Specification	ECAP Specification
T1*	**T_inicial**	***(none)***	***(none)***
T2*	**T004_M4**	**$\varepsilon = 0{,}04$; $\dot{\varepsilon} = 10^{-4}\ s^{-1}$**	***(none)***
T3	T006_M4	$\varepsilon = 0{,}06$; $\dot{\varepsilon} = 10^{-4}\ s^{-1}$	*(none)*
T4	T_inicial_CAP	*(none)*	4 passes, 473 K, 135°
T5*	**T004_M4_CAP**	**$\varepsilon = 0{,}04$; $\dot{\varepsilon} = 10^{-4}\ s^{-1}$**	**4 passes, 473 K, 135°**
T6	T008_M4_CAP	$\varepsilon = 0{,}08$; $\dot{\varepsilon} = 10^{-4}\ s^{-1}$	4 passes, 473 K, 135°
T7	T002_M4_CAP	$\varepsilon = 0{,}02$; $\dot{\varepsilon} = 10^{-4}\ s^{-1}$	4 passes, 473 K, 135°
T8	T018_M6_CAP	$\varepsilon = 0{,}18$; $\dot{\varepsilon} = 10^{-6}\ s^{-1}$	4 passes, 473 K, 135°
T9	T008_M6_CAP	$\varepsilon = 0{,}08$; $\dot{\varepsilon} = 10^{-6}\ s^{-1}$	4 passes, 473 K, 135°

Variables ε and $\dot{\varepsilon}$ represent the deformation load and strain rate, respectively. For the rectangular slabs, we have two control samples: one of them (*T1*) without any traction or SPD deformation, and another one (*T4*) being submitted exclusively to the ECAP processing. Despite that, samples *T1* (hot-rolling), *T2* (hot-rolling + tensile testing) and *T5* (hot-rolling + ECAP + same tensile testing) were chosen to be the main subjects of comparison towards progressive deformation steps.

As mentioned previously, characterization methods for sample analysis are synchrotron X-ray diffraction, along with optical metallography to directly observe the formation and increase of grain boundaries and interfaces through grain refinement. The method of choice for the analysis of the diffraction profiles was the manual verification by Gaussian adjustments, and simulation of the diffraction profiles was done via scripts written in MATLAB®.

3.2. MATLAB® simulation of kinematic scattering

The computational simulation of the Mg crystal lattice with and without defects and their respective XRD profiles follows a relatively simple execution line, composed of two main steps: (A) construction of the hexagonal close-packed lattice, and (B) simulation of the synchrotron X-ray scattering over the constructed lattice (*Figure 3.1*). All scripts developed are available in the Appendix of this dissertation.

The possibility to choose and adjust parameters such as the size of the atom matrix or the size of the inserted defect on the bulk material allows us to have some basic control over the processing time of the routine, which is helpful because it allows the use of very reduced matrices for performance testing and troubleshooting on the initial stages of conception of the code. Once the routine is established, we can then dramatically increase the size of the matrix and induced interfaces in an attempt to potentialize the scattered intensity - that would be the equivalent of an extended signal collection time in a real X-ray diffraction experiment.

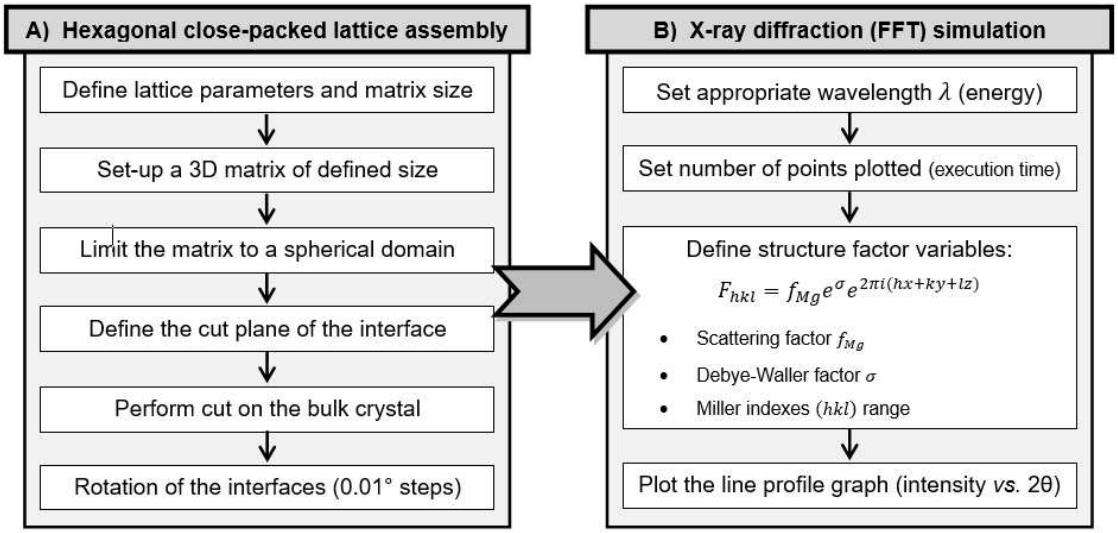

Figure 3.1 - Execution line diagram of the synchrotron XRD profile simulations.

Two Mg crystals with 30 x 30 x 30 unit cells are simulated with atomic positions following the bulk structure. The edge of these crystals is removed, making a sphere of atoms without any specific faceting in order to reduce form factor effects on the simulations [19,21]. After generating the spherical domain of atoms without defects (*Figure 3.2*), we can insert the defect by performing a cut of customizable size and thickness in the original lattice. By removing a slice of the perfectly organized lattice, rotating it accordingly and inserting it back in the lattice, we can create the desired interfaces on the crystal lattice. One thing to note is that the rotation of a point around an arbitrary axis is often computed as a set of many distinct matrix operations; however, it is possible to obtain a matrix that executes the rotation in a single operation, which is the *rotation matrix R* [42]:

$$R = \begin{bmatrix} \cos\theta + u_x^2(1-\cos\theta) & u_x u_y(1-\cos\theta) - u_z\sin\theta & u_x u_z(1-\cos\theta) + u_y\sin\theta \\ u_y u_x(1-\cos\theta) + u_z\sin\theta & \cos\theta + u_y^2(1-\cos\theta) & u_y u_z(1-\cos\theta) - u_x\sin\theta \\ u_z u_x(1-\cos\theta) - u_y\sin\theta & u_z u_y(1-\cos\theta) + u_x\sin\theta & \cos\theta + u_z^2(1-\cos\theta) \end{bmatrix} \quad (3.1)$$

This matrix governs the rotation of a given axis (defined at will) in the direction of a unit vector $\vec{u} = (u_x, u_y, u_z)$ where $u_x^2 + u_y^2 + u_z^2 = 1$, by an angle of θ. In this case, the main benefit of a single matrix operation is the significant reduction in computational time required to perform the rotation. In computational simulations where rotations will be performed in large numbers along with a multitude of other variables,

which is the case of this routine, having a practical computational time is a particular concern.

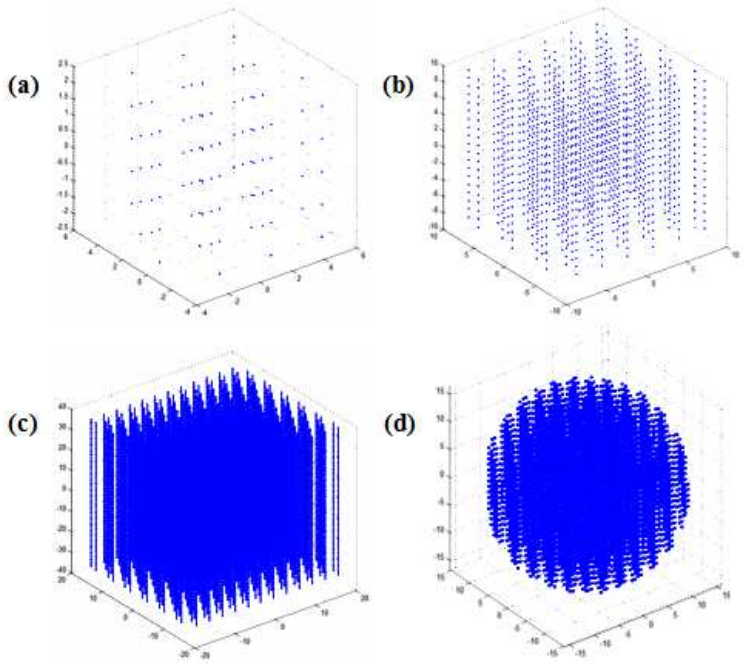

Figure 3.2 - Generation process of an approximate spherical lattice (MATLAB®).

The kinematical simulation of interface structures must make use, as a starting point, of the main symmetries and slip/twinning planes of the hcp system. Nevertheless, different interface structures can also be found [37–39]. In our simulations, we assume that abrupt interfaces take place between grains (although such occurrence does not apply to all interfaces). In such conditions, the permanence of a bulk lattice in the adjacent position of the interface plane, represented by a rotated crystal, gives rise to diffraction peaks that would not be observed in boundaries where amorphous or oxide grain contours take place. Therefore, aiming at identifying the occurrence of unexpected interface structures, our simulated crystals must present faceting occurring at angles in-between the main (highly symmetric) facets of an *hcp* system. Hence, the faceting planes of a simulated interface must be probed for a wide range of angular displacements with respect to three chosen slip and twinning planes of the *hcp* bulk system, namely the prismatic, pyramidal and tensile twinning planes [32], as indicated in Section 2.3.2. This is obtained by varying the cut planes according to the angles represented in *Figure 3.3*.

One of the crystals is left on a pre-defined orientation, while the other is rotated with respect to fixed axes that pass through the directions $[1\bar{1}0]$, [010] and [001]. The angles between the planes and the vertical *c* axis of a reference unit cell are hereafter named α and β, while the angle of the plane rotated azimuthally with respect to the *a* axis of the *ab* plane of the hexagonal unit cell is referred as γ. These angles are equal to zero at the (110) , (010) and $(1\bar{1}0)$ planes, respectively. All possible rotational configurations of the represented planes were scanned along the intervals between 0° and 90° for a and b, and 0º to 120º for g, with steps of 0.1°. The rotation of the cut planes was made perpendicular to the vector that is normal to the defined planes.

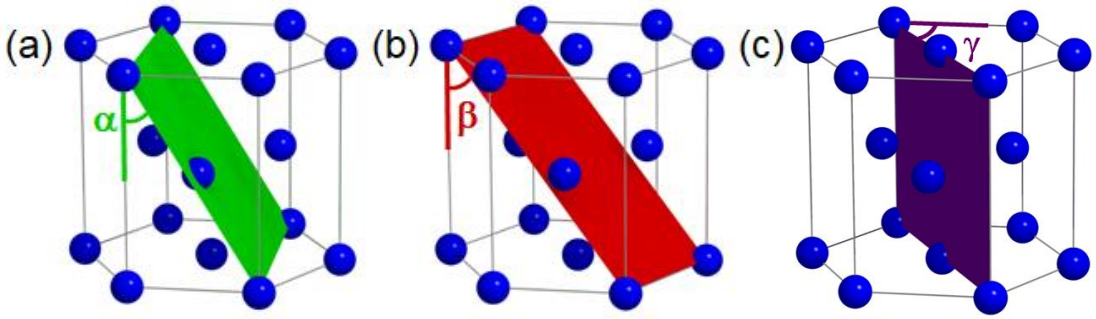

Figure 3.3 - Representation of the interface planes, defined as a function of the angles α, β and γ with respect to the (110), (010) and $(1\bar{1}0)$ planes of the *hcp* unit cell.

Finally, once the cut plane is determined and the rotations and insertions are done, we have the completed simulated hexagonal lattice with grain interfaces, as demonstrated in the example shown on *Figure 3.4*. From there, we can then simulate the diffraction profiles and compare them to the diffractograms of the hexagonal bulk lattice (that is, without the insertion of defects). A close-up example of the result is observed in *Figure 3.5*, where the atoms of the original bulk crystal are represented by blue spheres, while the inserted atoms of a rotated lattice are included as green spheres. The insertion has a finite size along one direction and spans over the whole crystal along two directions (a large slab). The interfaces obtained in such procedure are representative of extended grain boundary interfaces, or extended defects, that may occur inside our Mg samples.

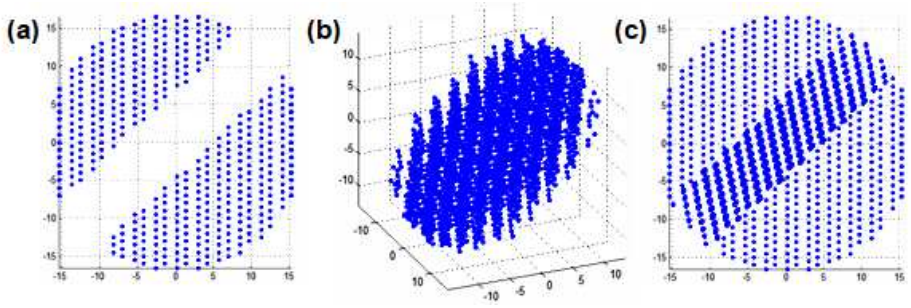

Figure 3.4 - Simulation of a defect in an approximate spherical lattice: **(a)** bulk cut, **(b)** rotation of the bulk slice and **(c)** insertion.

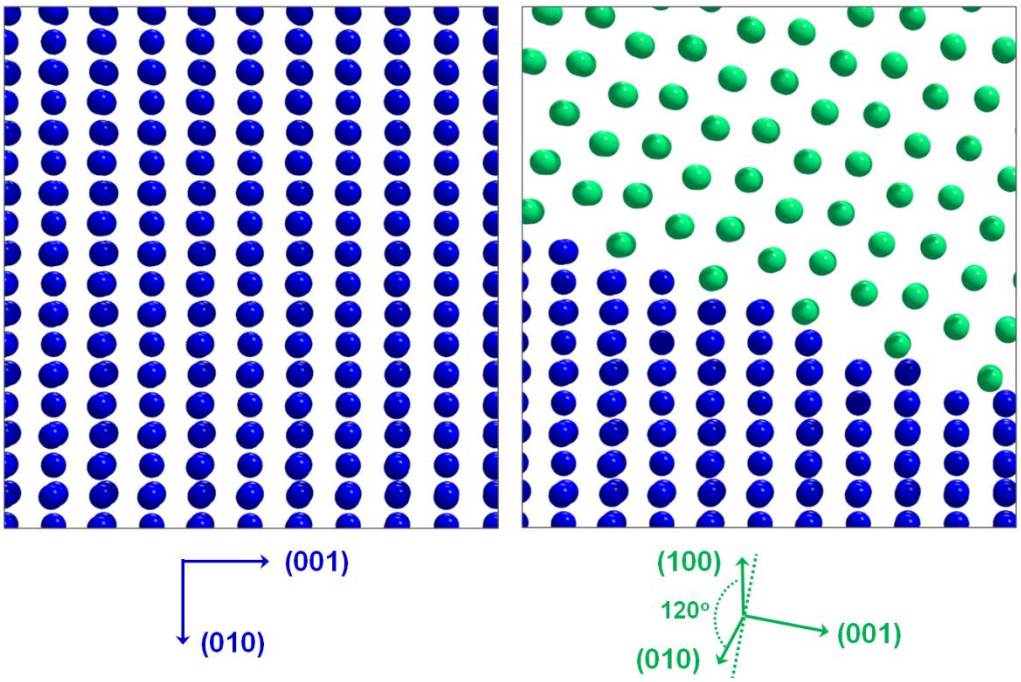

Figure 3.5 - Representation of a bulk Mg crystal with the *c*-axis along the horizontal direction (left panel). A rotated bulk crystal (green spheres) in inserted at its host matrix (blue spheres), generating two identical interfaces (right panel). *Note:* Atoms that appear superimposed at the interfaces are in fact displaced along the direction perpendicular to the represented figure plane.

3.3. Synchrotron X-ray diffraction experiments

X-ray diffraction data was acquired in the XRD1 beamline of the Brazilian Synchrotron Light Laboratory (LNLS – Campinas, São Paulo, Brazil). The full beamline layout consists of a white beam slit of 4 mm, a vertical focusing mirror, a Si(111) double crystal monochromator and physical slits of 4 mm and 2 mm (*Figure 3.6*), having a total

length of 18,2 m between the beam output (by the bending magnet) and the experimental station. The bending magnet acts as a source from which a monochromatic 12 keV (which corresponds to a wavelength of $\lambda = 1.03293$ Å) beam with an integrated flux of 10^{11} photons/s comes out, focusing at the sample position with a spot size of 3 mm x 0.7 mm. The experimental station incorporates a Newport® 3-circle diffractometer (N3050-P1) with a maximum amplitude of 150°, and a Mythen 24K linear detection system from Dectris® consisting of 30720 channels that cover an angular range of 120°. The Mg samples were illuminated at a fixed incident angle of 10°, resulting in a penetration depth of approximately 100 μm. For this penetration depth, the formation of native oxide on the sample surface is negligible. Our acquisitions were restricted to a maximum integration time of 3600 seconds (one hour) and the oxide layer on the sample surface is removed immediately before measurements. In order to fill up detection gaps of the detector array, two acquisitions with a 0.5° difference were carried out for each sample. The intensity profile is then extracted using the dataset from the second acquisition for angular intervals without data at the first scattering angle. Data acquisition was done using a Red Hat workstation with the Py4Syn python package, developed at LNLS.

Figure 3.6 - XRD1 beam line layout (LNLS archive).

Preparation of the magnesium samples was relatively simple, following only a polishing step with fine-grained sandpaper sheets (600 and 1200 grit sizes) and coating with a thin Kapton® adhesive tape to prevent any formation of oxide layers on the surface of the samples that could manifest in the diffraction patterns (*Figure 3.7*). The Kapton® polyimide film is a good barrier material useful in various systems, and has a low enough crystallinity so that its diffraction pattern is negligible when added to the sample of interest [46].

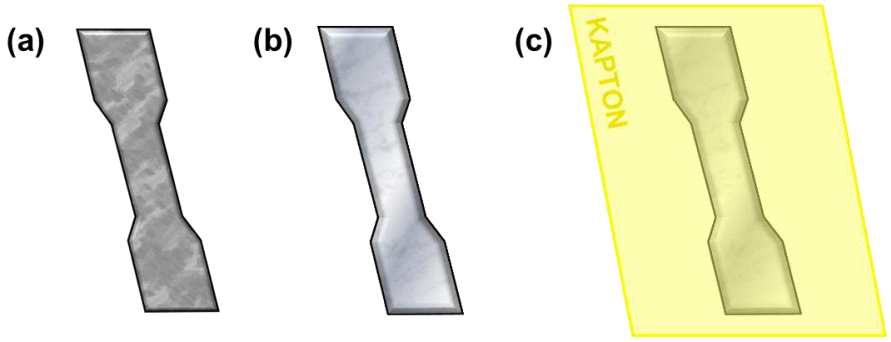

Figure 3.7 - Simplified representation of the rectangular slab samples evaluated: **(a)** in its initial state with specified mechanical processing, **(b)** after polishing, and **(c)** attached to the Kapton® tape and on to the diffractometer.

4. RESULTS

4.1. Magnesium Sample Overview

A first overview of our samples is provided by optical metallography, depicted in *Figure 4.1*. The optical microstructure of the commercially pure Mg ingot is shown in *Fig. 4.1(a)*, which exhibits large grain sizes (~300 μm). *Figs. 4.1(b)* and *(c)* represents the hot-rolled (*T1*) and hot-rolled submitted to tensile test (*T2*) samples respectively, whereas *Fig. 4.1(d)* depicts the sample processed by hot-rolling and ECAP followed by tensile test (*T5*). One notices that the grain size is considerably reduced (in the range of tens of microns to a few micrometers) when subjecting the samples to rolling and ECAP processes, creating a large amount of interfaces with a consequently larger and more random distribution of interface orientation [27]. For Mg, it is known that untreated grain sizes of the order of 300 microns are commonly retrieved, while treatments such as ECAP and traction/compression reduce the grain sized to tens of micrometers.

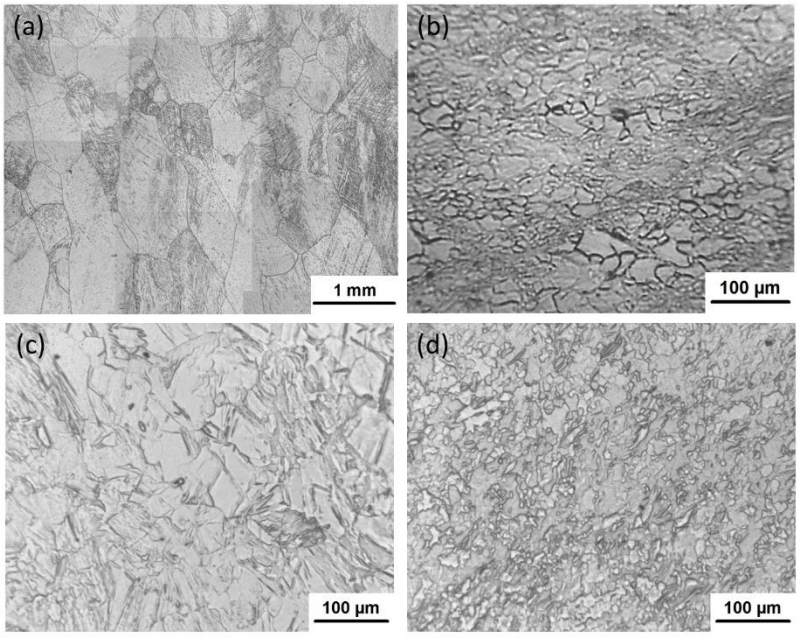

Figure 4.1 - Optical metallography images of Mg samples in four distinct conditions: **(a)** as-cast sample, **(b)** hot-rolled sample (*T1*), **(c)** hot-rolled sample subjected to a tensile test (*T2*), and **(d)** hot-rolled, processed by ECAP, and submitted to a tensile test (*T5*). The experimental parameters of the tensile tests were similar for samples exhibited in (b) and (c).

4.2. Synchrotron X-ray diffraction of *hcp* materials

Figure 4.2(a) shows a sketch of the synchrotron XRD setup used. The simulated diffractogram of bulk Mg based on a reference crystal structure [47] corresponds to the blue XRD pattern exhibited in *Figure 4.2(b)*, where all the observed peaks respect the rules of structure factor extinction for the *hcp* lattice (i.e., fundamental peaks) [41]. The experimental data recorded in our setup for the sample *T2*, subjected to hot-rolling and tensile test, is shown in red in *Figure 4.2(b)*, where arrows mark the presence of peaks which do not correspond to the bulk material diffraction. The distinct intensities between fundamental peaks is ascribed to texture effects on the measured sample (simulated data stands for a powder with random domain orientations). Despite only showing the XRD profile for one of the samples, it's important to note that all nine samples exhibited the same non-corresponding peaks, only with distinct relative intensities. This fact will come in hand in the discussion section later on.

A zoom of selected angular regions pointing the most intense additional peaks observed is provided in *Figure 4.2(c)*. The retrieved additional peaks are located close to the Mg (102), (200), (204) and (300) reflections. We have carried out a careful analysis of Mg oxides, and their diffraction peaks do not occur for angles where additional peaks were retrieved. Oxide peaks coming from a thin layer at the surface are also known to be broad, if the compound is crystalline, or to appear as a smooth background at lower scattering angles if the compound is amorphous. The presence of impurities (such as Si) and their possible clustering into intermetallic was also not observed. Such peaks are then related to extended atomic configurations (interface core) inside polycrystalline Mg. Since grains are individual single crystals, the regular atomic configurations that generate diffraction peaks which are not bulk-related can only be found in interfaces such as grain boundaries, subgrain boundaries, twin boundaries, and twist transition boundaries [9–11].

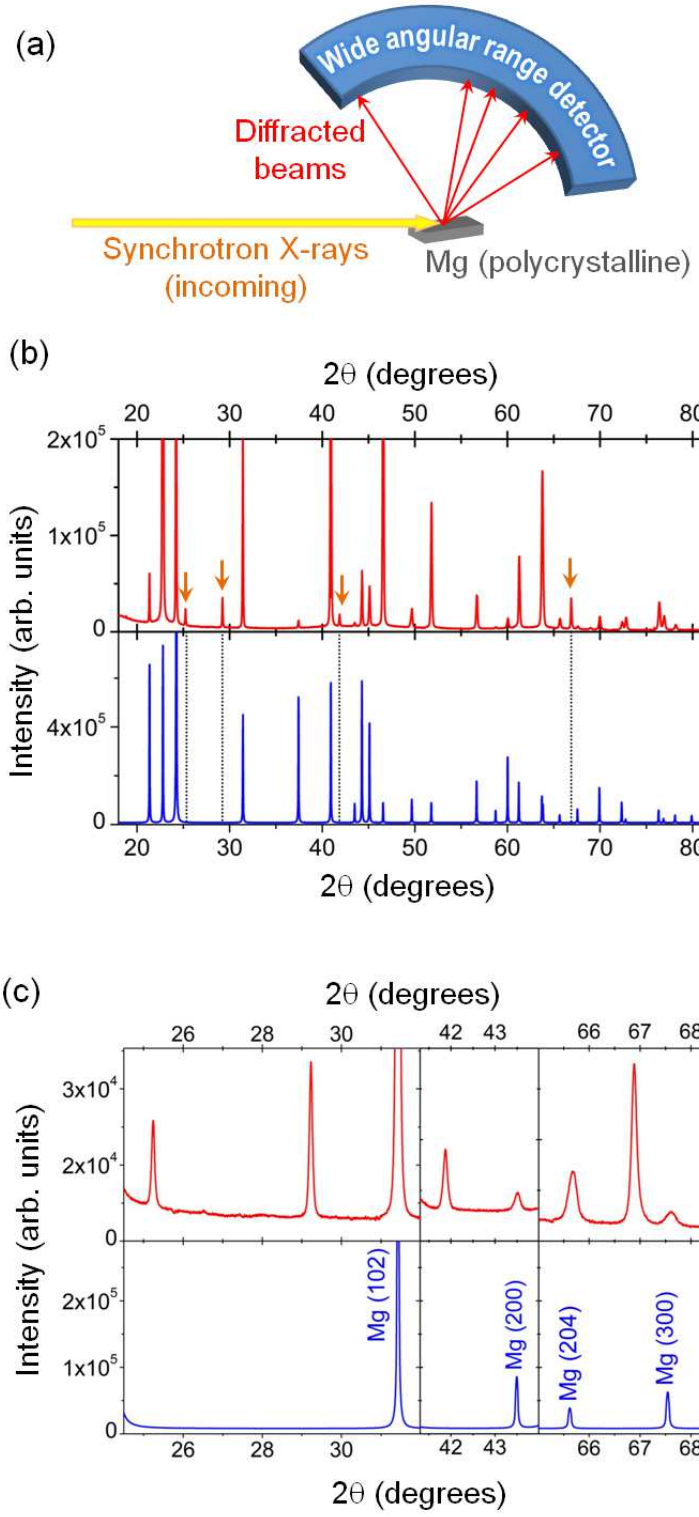

Figure 4.2 - **(a)** Sketch of the diffraction setup used, with a long linear detector (24 x 1280 channels). **(b)** Measured (upper panel, red curve) and simulated/bulk (lower panel, blue curve) diffraction profiles for Mg. **(c)** Selected regions of the diffractograms for the measured (upper panel) and simulated/bulk (lower panel) diffraction profiles.

After measuring the CP-Mg samples, we have the raw, full synchrotron XRD profiles collected for all nine samples, shown in *Figure 4.3*:

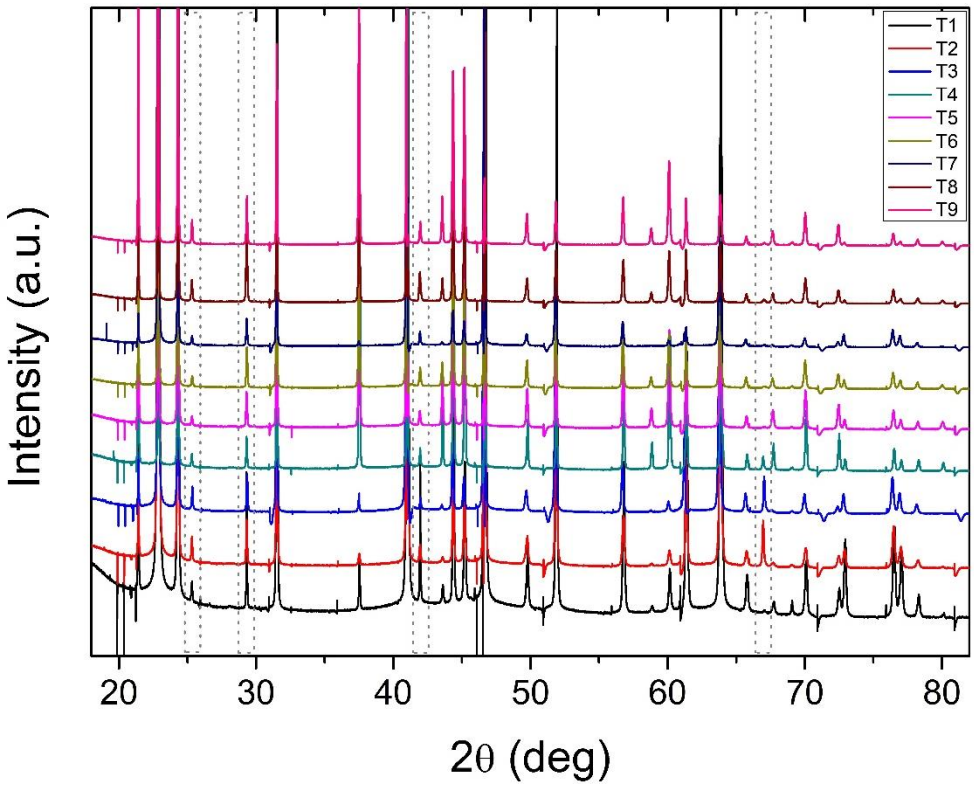

Figure 4.3 - Overview of raw data synchrotron XRD profiles for all nine CP-Mg samples. The dotted lines mark the position of additional peaks observed.

Indexing and interpretation of the characteristic peaks for the Mg crystalline structure can be done through several different methods, such as by comparison using diffraction patterns from databases, or automated analysis through the use of phase identification software (HiScore Plus, Match!, etc). This type of software basically works under the same method of comparison, but can also provide data processing, calculation of phase percentages (for composite materials), etc. Here, we chose to use the method of direct comparison using a diffraction pattern obtained through the Crystallographic Open Database (COD) [47] and presented with PowderCell software [48]. The whole set of samples corresponds well to the database standards, and aside from the aforementioned non-fundamental peaks highlighted in *Figs. 4.2* and *4.3*, no peaks corresponding to other materials or possible oxide formations were observed.

By making Gaussian fittings to these specific reflection peaks, we could extract parameters such as width at half height (FWHM), height or integrated area that would allow for the inferring of information about, for example, grain sizes and asymmetries that characterize different types of defects generated inside each sample after the deformation tests. However, being that these samples are polycrystalline but not *actually* powdered, the relative intensity of the additional peaks could, in part, be associated with innate texture effects induced when choose a specific orientation/placing of the samples on the diffractometer (see *Fig. 3.7*). Therefore, it could not be a fully reliable source data to evaluate.

With that being said, having the XRD profiles of the actual Mg samples in hand and extracting the parameters of the reflection peaks of interest enables us to associate them with the previously proposed computational simulation, at least in a qualitatively level, in an attempt to reproduce the conditions in which we observe the peaks suggested as induced by defect formation. If that can be done, we can therefore verify the possible configurations of interfaces and try to offer explanations regarding the formation process of those defects with respect to the planes of occurrence, predicted microstructural characteristics and properties, among others aspects.

4.3. Simulating XRD profiles for a perfect *hcp* lattice

Firstly, a kinematical simulation of a bulk Mg crystal was carried out in an attempt to verify the accuracy of the simulation routines in comparison with the XRD profile of a real Mg bulk. This means interfaces were not introduced.

The diffraction of simulated crystal lattices with and without the insertion of grain interfaces were obtained for the scattering amplitude of all relevant sets of (hkl) planes (00L, 01L, 10L, 11L, 20L, 21L e 30L), up to the imposed limit where $l = 9$. The simulation of planes with Miller indexes beyond this value would be unnecessary, since Bragg peaks for those reflections would appear at angular positions that were out of the reach for the beamline detectors on the real samples (in other words, we couldn't observe past this point with the current experimental setup).

After simulating the scattering amplitude for all sets of planes using an energy of $\lambda = 1.03293$ Å (the same used on the experimental measurements), all of the simulated profiles were merged into a complete diffractogram for a Mg bulk. It was seen that the simulated Bragg peaks for the perfect crystal lattice were highly corresponding in their angular positions (2θ) when compared to the reference diffraction pattern [47]. The only factor that differentiates the simulated diffractogram from the database reference is the non-inclusion of the *multiplicity factor* in the calculation of the hexagonal lattice structure factor, which was not considered essential until the present stage of study. The multiplicity factor was not incorporated since relative proportion of *hkl* planes is not of interest, and also not to interfere or cause incorrect interpretations of the integrated intensity values for single, non-fundamental reflections that have no correspondence with integer Miller indexes. This choice was maintained when incorporating the grain interfaces into the simulated lattices.

4.4. Simulating XRD profiles for an *hcp* lattice with grain interfaces α, β and γ

The primary objective for these simulation routines was to verify the occurrence of scattered amplitudes that could be attributed exclusively to the insertion of defects (being it grain boundaries, twin boundaries, or any other interfacial structure). Subsequently, the objective is to try specifying an interface (cut) direction that produces diffraction peaks as close as possible to those observed in the real CP-Mg samples.

As the angles and inclusion interfaces α, β and γ are varied, we find out which configurations produce diffractions peaks with appreciable intensity at similar positions where additional peaks were observed in the measurements of, e.g., *Fig. 4.2(b)*. We must mention here that many configurations of rotation and interface inclusions do not produce any additional diffraction peaks, while others produce peaks at positions in the diffractogram where no appreciable intensity was measured above the background.

The diffraction intensity from our computer-generated matrix of atoms is retrieved by the kinematical relation:

$$I(q) = \left| A_o \sum_i f_{Mg,i}(q) e^{-\sigma^2 \boldsymbol{R}_i^2 / 2d^2} e^{i\boldsymbol{q}.\boldsymbol{R}_i} \right|^2 \quad (4.1),$$

where q is the reciprocal space condition in which the scattering intensity is evaluated, A_0 is a constant used for normalizing the total scattering intensity, $f_{Mg,i}(q)$ is the atomic scattering factor of the Mg atom at position i, σ is an effective fluctuation of the defect/host crystal interface position, set to 2.0, which allows for broadening of the profile and reduction of finite size oscillations from the simulated interfaces, and d is the Mg-Mg atomic distance considering a bulk hard sphere model ($d = 0.321\ nm$).

Some configurations retrieved that simulate observed peaks are unambiguous and univocal, while in other cases the observed peaks can be obtained by more than one interface configuration (atomic arrangement and periodicity). In the next paragraph we provide details of the simulated outcome, while in the following we establish conditions to infer the most probable interfaces in cases where two or more geometric conditions give rise to non-fundamental diffraction peaks.

Since all additional, non-fundamental peaks appear below $2\theta = 80°$ (see *Fig. 4.2*), our simulated scattering range was limited to this angle. As the cut/rotated crystal is inserted into the host original matrix with angles near a specific interface that generates additional scattering peaks, some intensity is observed. The incoming simulated peak has an onset and then drifts in 2θ, generally achieving a maximum intensity at a specific position. After this point, the simulated peak drifts along a similar range while its intensity starts to decrease, vanishing afterwards. Such set of conditions establish a range of possible interface angles and a maximum strain condition, which can be understood as the difference between the interplanar spacing retrieved experimentally (from the 2θ angle value) and the corresponding d-spacing obtained from the peak intensity of the simulated interface (which makes use of bulk lattice parameters). We assume here that near the interface core (in the adjacent bulk material) the lattice parameters a and c do not differ considerably from those measured in bulk Mg. *Figure 4.4* shows a comparison of a simulated peak (blue line) and a measured non-fundamental peak (red line). In this figure, the width of the simulation peak and its lateral intensity oscillations are due to the finite crystal size. Despite of its broader profile, the simulated peak width still allows one

to distinguish them from any neighboring peaks observed experimentally. An example of a simulated peak is provided in *Figure 4.5(a)*. Here, the non-fundamental peak observed experimentally at the scattering angle 2θ = 67.02° is retrieved on the simulation with a maximum intensity at 2θsim = 66.93°. It can be seen that the simulated intensity is significant for interface angles α spanning from 29.5° to 32.8°. The maximum of the simulated intensity is compared to the maximum of measured intensity in *Figure 4.5(b)*, showing that a relatively low strain with respect to a bulk configuration is obtained.

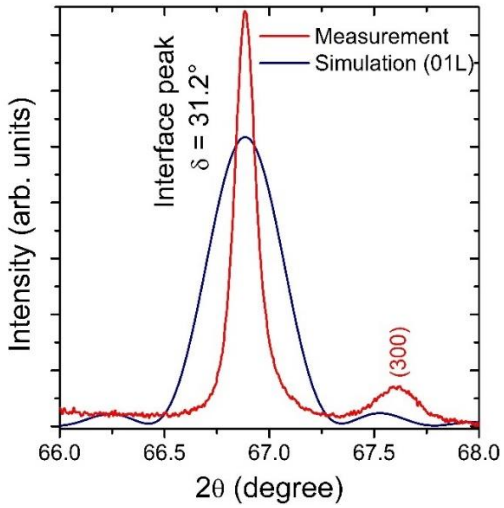

Figure 4.4 - Experimental (red line) and simulated (blue line) interface peaks. The larger width and side maxima observed in the blue curve are due to the finite size of our simulated crystal.

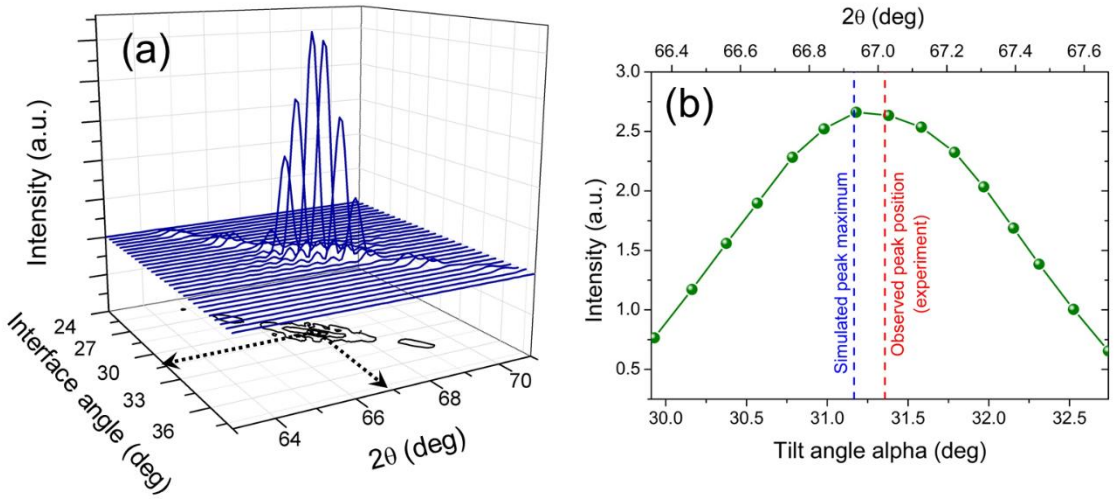

Figure 4.5 - (a) Simulated intensity profile for interface peak at 2θ = 67.02° plotted with respect to the interface angle and scattering angle (2θ). **(b)** Detailed view of the observed maximum intensity for the tilt angles used for the α plane interface near 31.2°.

Simulations were carried out for the cutting planes indexed by the angles shown in *Figure 3(a)*, as stated previously. Steps of 0.01° on interface tilt angle were used along a 90° range for α and β and 120° range for γ. Additional peaks were not observed for variations in the γ angle, while several conditions of α and β were capable to produce diffraction intensity along the 2θ range. The retrieved conditions of inserted rotated crystal slabs that lead to the occurrence of one (or more) interface peaks in the diffractogram are listed in *Table II*. We have gathered the information of the experimental and simulated peak position in 2θ (scattering angle), the type of rotation (α, β or γ planes), the angle of rotation of the inserted crystal (that creates the interface), the maximum estimated strain (considering a simplified bulk one-dimensional distortion), the interface angular tolerance, and the corresponding peak spread in 2θ. For the experimental peaks with more than one possible interface structure (2θ = 29.32° and 67.02°), the relative intensity of the simulated peaks is also depicted in the third column of *Table II*. Only simulated peaks with an estimated strain differing less than 2% are listed here. Finally, we have also simulated stacking faults [49] in which the ABAB registry along the *c* (00L) axis is replaced by ABCAB (local insertion of a [111] FCC plane) and ABBA stackings, and the known $\{10\bar{1}2\}$ twin in Mg [32]. These simulations do not reproduce any of the observed peaks.

The most probable configurations for interfaces that generate the observed peaks are indicated by bold characters in *Table II*. While for the measured peaks at 2θ = 29.32° and 41.95° the lowest strain solutions observed are compatible with both the peak position (experimental) and the maximum simulated intensity (theory), the peaks at 2θ = 25.33° and 67.02° have non-trivial solutions. For the lowest angle peak (2θ = 25.33°), only one solution was retrieved, with a large interface angle tolerance. In this case, where the simulated peak intensity is shown in *Figures 4.6(a)* and *4.6(b)*, the 2θ angle of the intensity maximum of the simulation would require a highly strained interface. Nevertheless, one can assume that the energy minimization for this interface takes place for the interface angle that corresponds to a near zero strain condition (informed between parentheses in the second line of *Table II*), still producing an appreciable intensity at this specific scattering angle. For the highest angle peak (2θ = 67.02°), the simulated peak that corresponds to the minimum strain condition (0.08% compressive) presents a very

low intensity if compared to a much more intense condition that takes place at 0.12% compressive strain. We therefore assume that this second solution (which was shown in *Fig. 4.5*) is the most probable to induce the appearance of a strong experimental interface peak, such as the one observed in sample *T2* shown in *Fig. 4.2(b)*. Three of the interface conditions selected as probable ones are originated by α-type interface planes, while only one is obtained from a β-type interface plane.

Table II - Experimental and simulated peak positions for interfaces (first and second columns). All retrieved conditions that lead to an estimated strain of less than 2% with respect to bulk interface configurations are listed (except for the 25.33° peak, see text for discussion). The relative intensity (with corresponding interface plane), interface angles and estimated strain of the experimental peak with respect to the bulk simulated configuration are depicted in the third, fourth and fifth columns, respectively. The sixth and seventh columns of the table exhibit the angular tolerance in the interface angle (range for which at least 10% of the simulated peak intensity is still observed) and its angular spread along the diffraction (2θ) angle.

Experimental peak position 2θ (degrees)	**Simulated peak position 2θ (degrees)**	**Relative intensity/ Interface plane**	**Interface angle (degrees)**	**Estimated strain (%) (max. sim.)**	**Interface angular tolerance**	**Peak spread in 2θ (simulation)**
25.33°	**24.445° (25.330°)**	**1 (β)**	**62.10° (63.32°)**	**-3.44 (0)***	**3.60°**	**2.23°**
29.32°	**29.321°**	**1 (α)**	**30.162°**	**0.003**	**12.00°**	**0.09°**
	29.609°	0.048 (α)	39.775°	0.97	5.48°	0.20°
	29.632°	0.009 (β)	39.162°	1.04	1.93°	0.21°
41.95°	**42.106°**	**1 (α)**	**40.802°**	**0.35**	**3.15°**	**0.69°**
67.02°	66.958°	0.007 (β)	44.023°	-0.08	2.01°	2.12°
	66.927°	**1 (α)**	**31.179°**	**-0.12**	**3.72°**	**1.69°**
	66.850°	0.081 (β)	23.448°	-0.22	3.81°	1.38°
	66.773°	0.066 (β)	73.059°	-0.33	1.28°	3.77°

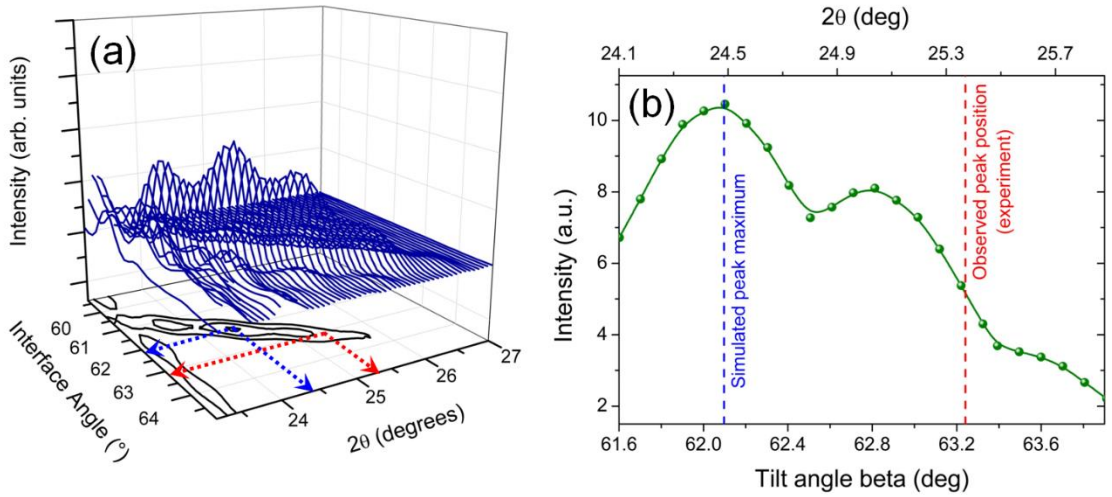

Figure 4.6 - (a) Simulated intensity profile of the interface peak at 25.33° plotted with respect to the interface angle and scattering angle (2θ). The intensity observed at the left corner is due to the proximity of the (002) bulk peak. In this case the maximum of the simulated intensity does not match the 2θ position of the experimentally observed peak with low strain values. Nevertheless, the interface angle can be tuned to a value where considerable diffraction intensity is still observed, yielding a peak at the measured 2θ position for a β-type interface. **(b)** Detailed view of the observed 2θ maximum intensity for the tilt angles used for the β plane interface near 62.5°, indicating the maximum simulated intensity peak and the observed interface peak position.

Similarly to *Figs. 4.5* and *4.6*, the intensity of the forbidden peaks observed at 2θ = 29.32° and 2θ = 41.95° as a function of the interface tilt angle are shown in *Figures 4.7(a)-(d)*. These are cases of unambiguous or univocal solutions, as it can be seen by its retrieved data in *Table II*.

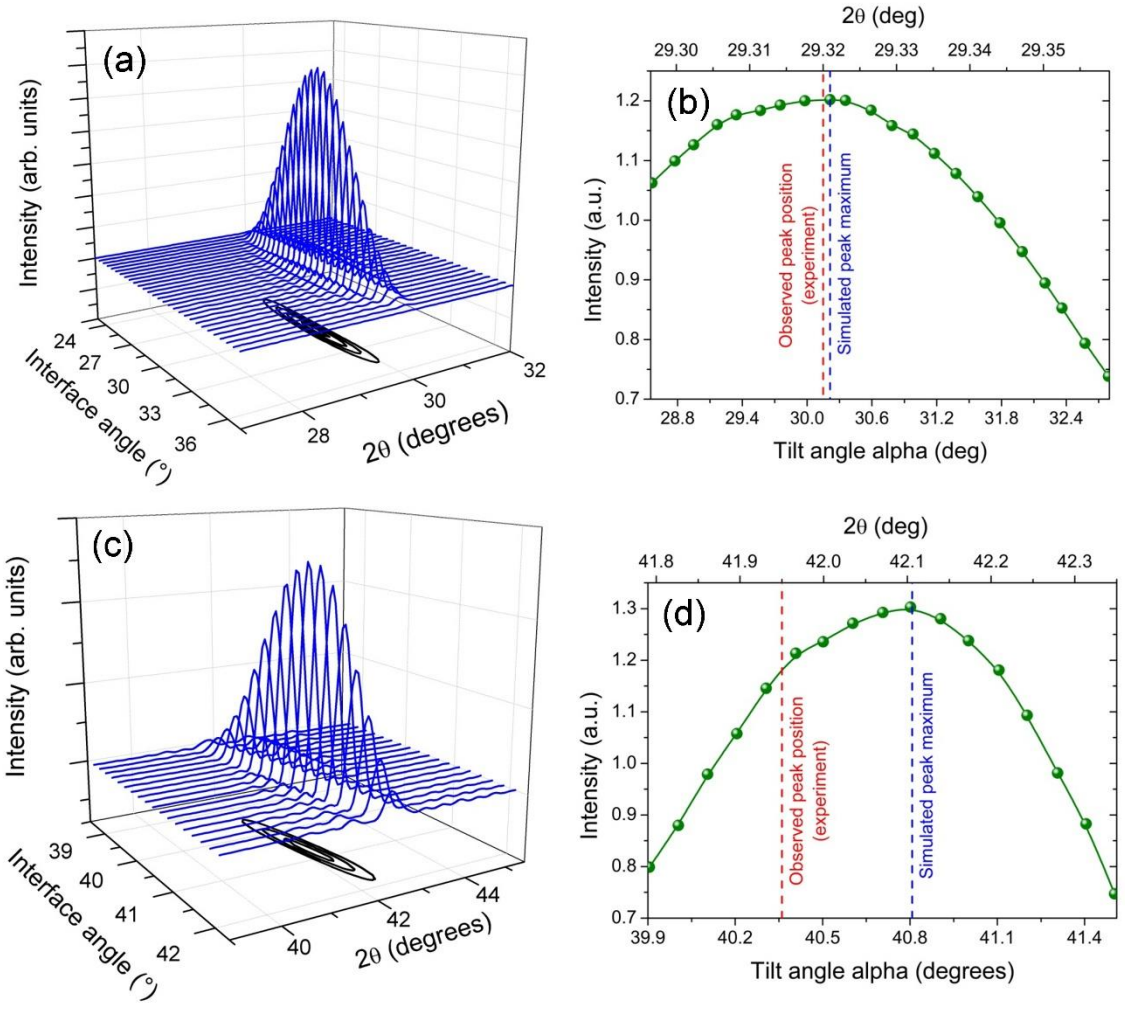

Figure 4.7 - (a) Simulated intensity profile for the interface peak at 2θ = 29.32° plotted with respect to the interface angle and scattering angle. **(b)** Detailed view of the simulated maximum intensity. **(c)** Simulated intensity profile for the interface peak at 2θ = 41.95° plotted with respect to the interface angle and scattering angle. **(d)** Detailed view of the simulated maximum intensity.

5. GENERAL DISCUSSIONS

The most probable interface structures for each of the non-fundamental peaks retrieved experimentally from our XRD methodology are represented schematically in *Figure 5.1(a-d)*. In this figure, atomic configurations for the conditions marked in bold in *Table II* were graphically generated by a MATLAB® script and visualized in POV-Ray™. The axis of crystallographic planes for the bulk matrix (blue) and the interfaced crystal (other colors) are also shown. One notices that the distinct patterns in the interface line are retrieved. Their geometry may be related with conditions that lead to local energy minimization with a symmetry that allows for XRD, representing a long-range ordered pattern of atomic distributions in Mg. One must recall here that other interface conditions also produced diffraction intensities, but in regions of the diffractogram where no additional peaks were experimentally observed. Therefore, our solutions do not rule out the existence of interfaces with reduced symmetry (i.e., interfaces that do not generate X-ray peaks), but rule out the occurrence of highly symmetric configurations in our samples, such as commensurate configurations (superstructures) at the grain interfaces. It is also important to notice that the interfaces observed here are extended ones, since all additional (non-fundamental) peaks measured are considerably sharp. No signal of interfaces with reduced size (broad peaks) were measured.

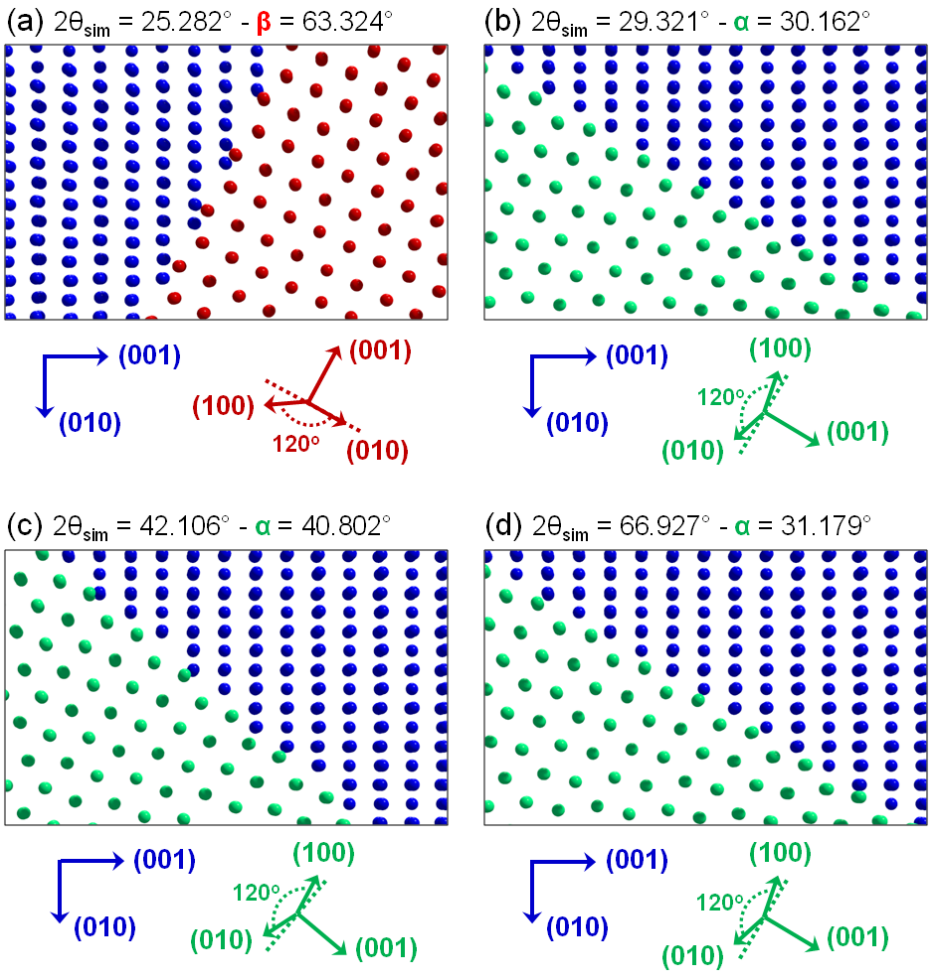

Figure 5.1 - Representation of the most probable Mg grain interfaces that generate additional XRD peaks in our measurements. *Note:* Atoms that appear superimposed at the interfaces are in fact displaced along the direction perpendicular to the represented figure plane.

We make use of the idea of observing Mg interfaces by XRD to compare the interplay of interface relative volume and the condition of pure Mg samples after mechanical processing. *Figure 5.2(a)* shows the full simulated diffractogram, with the non-fundamental peaks marked with arrows. Selected samples *T1*, *T2* and *T5* are shown in panels *Fig.5.2(b-d)*, providing an overview of interface behavior after mechanical processing. In *Fig. 5.2(b)* we show a measurement of a hot-rolled Mg sample (*T1*). For this condition the interface peaks at 29.32° and 41.95° are quite intense with respect to the interface peaks at 25.33° and 67.02°. A tensile strain of $\varepsilon = 0.04$ at a rate of $\Delta\varepsilon = 10^{-4}$ s^{-1} was then applied to the sample (*T2*). The results, already exposed in *Figure 4.2*, are reproduced in *Figure 5.2(c)*. After tensile tests, one observes the reduction of the

diffraction from α-plane interfaces at 29.32° and 41.95°, indicating that the re-orientation of grains takes place reducing the overall presence of these types of interfaces. On the other hand, tensile strain enhances the signal of peaks at 25.33° (β plane) and 67.02° (α plane), which points out to an increase in the overall population of such interfaces. Finally, the same tensile test was applied to the hot-rolled sample after ECAP processing (*T5*), and the diffractogram of *Figure 5.2(d)* was measured. ECAP is known to be a severe plastic deformation technique that produce ultrafine grain size and a consequent increase in the interface's density in metals and alloys [23,32]. Therefore, the relative reduction in the population of both α-like and β-like interfaces that induce the appearance of the measured peaks might be explained by the introduction of novel configurations of interfaces. Besides that, the XRD results can be compared to the metallography images of *Figure 4.1*, where ECAP refines the grain size but still leaves micrometer-sized interfaces, justifying the experimental interface diffraction peak width in our experiments (a coherence length of approximately 2 μm is produced at the bending magnet source used here).

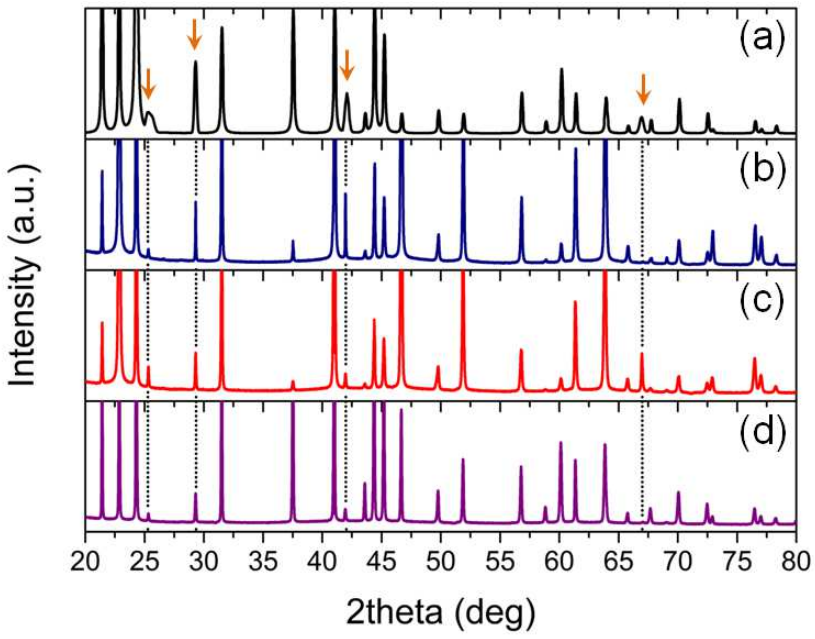

Figure 5.2 - (a) Simulated diffractogram for a crystal containing the four most relevant interfaces described in Table I. **(b)** XRD measurement of the hot-rolled Mg sample (*T1*). **(c)** XRD measurement obtained under the same conditions for the rolled sample subjected to tensile strain $\varepsilon = 0.04$ with rate $\Delta\varepsilon = 10^{-4}\ s^{-1}$ (*T2*). **(d)** XRD measurement for the rolled sample subjected to the same tensile strain/rate as (c) after ECAP processing (*T5*).

Figure 5.3 shows the relative intensity of the four retrieved forbidden peaks, displayed with respect to the processing procedure applied to the samples of *Figure 5.2*. Although a quantitative comparison is not recommended here (as it was said in *Section 4.2*, samples have distinct textures), large changes on all peak intensities can be ascribed to the reduction of the total volume of grain boundary interfaces that diffract at these peak positions.

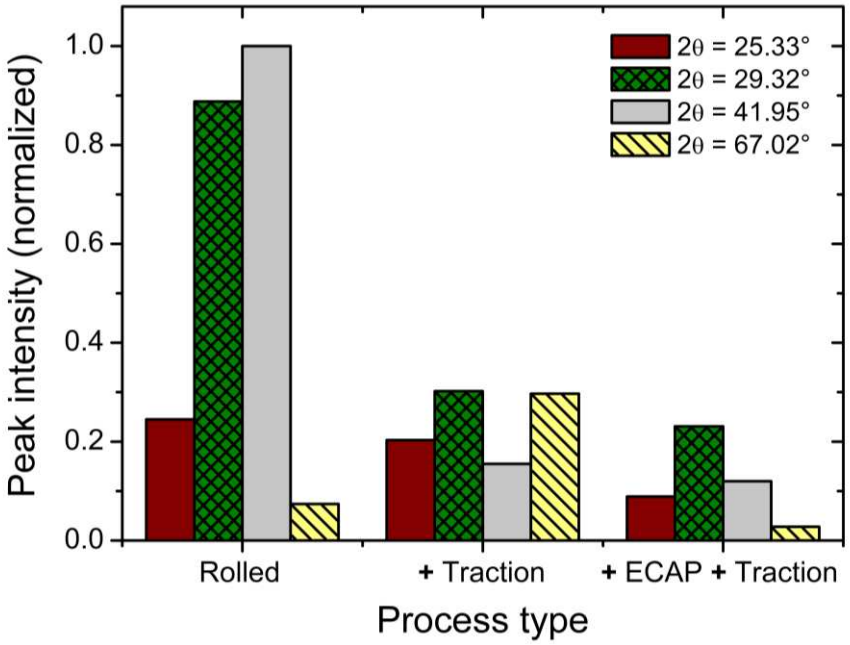

Figure 5.3 - Relative intensity of forbidden peaks as a function of processing type.

Interesting considerations concerning our results can be drawn in the perspective of recent works that evaluate the orientation and energy of symmetric and asymmetric tilts of grain boundaries. A work by Silva et. Al. [50] showed that high-pressure torsion (another SPD technique that induces UFG formation) applied to Mg samples can generate grain boundaries with low misorientation angles that average at about 30°; that seems to be compatible with one of the retrieved interfaces in this work, despite not providing further information that could confirm the exact preferential interface of those grains. The energy of symmetric grain boundaries was evaluated by molecular dynamics by Wang et. al. [38]. Their modelling is based on tilting both sides of Mg and Ti crystals varying the equivalent of our β angle. They found that besides the endpoints (0° and 90° tilts with respect to the *hcp c*-axis), local minima of the grain boundary configuration energy are retrieved in four specific tilt angles. Ostapovets and Sheikj-Ali proposed, more recently,

that asymmetric configurations (a distinct tilt for each side of the grain boundary) would lead to smaller energies than symmetric tilts [39]. This finding is in agreement with our retrieved interfaces, shown in *Figure 5.1* as a result of X-ray non-fundamental peak analysis. A more complete scenario was obtained by Zhu et. al., using an evolutionary search algorithm [51]. In this last work, asymmetric interfaces were found and classified into families in which the sharp discontinuity of grain boundaries is observed without the presence of atomic voids observed for the symmetric case. All these simulations point out, albeit of their restricted direct applicability to materials in real non-equilibrium thermodynamic conditions (with $T > 0$ K), that interfaces such as those retrieved in our work may be less energetic than usually investigated twin-plane conditions. We believe our results are a first glimpse of what can be produced in new generation synchrotrons with wide-range detection systems, which will surely extend the applicability of the method and provide interesting feedback for a broad spectrum of research ranging from ab-initio theoretical calculations to applications tuning properties of polycrystalline materials.

6. CONCLUSIONS

We have shown in this work that a kinematical modeling consisting of a rotated hexagonally close-packed lattice for Mg divided in two domains with an interface can be used to verify that non-fundamental diffraction peaks may arise from grain boundaries and interfaces. In our model, the boundary interface angle is varied in small steps for the main planes of the system and the diffraction intensity profile is simulated. We are able then to infer the preferential interface conditions for Mg, with information about the maximum strain at the interface plane with respect to a pure bulk configuration.

The obtained diffractograms with progressively increasing intensities of defect-induced peaks show that the proposed and assembled simulation routines can reproduce effects caused by local distortion of lattice parameters on the scattered intensities with relative reliability, which gives us greater confidence when expanding the simulations to different orientations or configurations of defects. The use of simulations, although limited in terms of computational capacity, gives us an advantage in the sense that, once consolidated for the *hcp* structure, the calculation routines can be adapted not only to other crystal arrangements and interface orientations that are often reported in literature, but to more complex crystalline systems like the rhombohedral or triclinic crystals, etc. It would also be interesting to extend the simulation routines to make it easily adaptable to other types of crystalline lattices and other types of analysis, such as the simulation of diffraction maps in reciprocal space rather than line profiles, or the joint study of more than one type of crystalline defect at a time.

The knowledge of X-ray peaks arising from interfaces allows for monitoring changes in a system when it undergoes mechanical processes that refine grain sizes and modify grain orientation (for instance). Contrary to most of the microscopy results explored in the field (optical microscopy, electron microscopy, atomic force microscopy) X-rays are sensitive to buried grains. Such inherent characteristic drives the method beyond the microscopy surface analysis, providing at the same time statistical relevance (due to large area illumination) and depth capabilities (incident angle can be modified in a polycrystalline sample). Metals, alloys and other polycrystalline materials may benefit

from this perspective, where the existence of a population of a given interface can be maximized or minimized to retrieve desired mechanical/chemical/physical properties.

FINAL REMARKS

This research has been supported by "Conselho Nacional de Desenvolvimento Científico e Tecnológico (CNPq)," "Coordenação de Aperfeiçoamento de Pessoal de Nível Superior (CAPES)," and "Fundação de Amparo à Pesquisa do Estado de Minas Gerais (FAPEMIG)" through research grants and scholarships. This research also used resources of the Brazilian Synchrotron Light Laboratory (LNLS), an open national facility operated by the Brazilian Centre for Research in Energy and Materials (CNPEM) for the Brazilian Ministry for Science, Technology, Innovations and Communications (MCTIC). The XRD1 beamline staff is acknowledged for the assistance during the experiments.

REFERENCES

[1] C. Zhu and B. Chen, “Atomic Scale Investigation on Precipitates and Defects of Mg–RE Alloys: A Review,” *Advanced Engineering Materials*. 2019.

[2] T. T. T. Trang *et al.*, “Designing a magnesium alloy with high strength and high formability,” *Nat. Commun.*, vol. 9, no. 1, 2018.

[3] Z. Zeng, J. F. Nie, S. W. Xu, C. H. J. Davies, and N. Birbilis, “Super-formable pure magnesium at room temperature,” *Nat. Commun.*, 2017.

[4] Y. Huang and T. G. Langdon, “Advances in ultrafine-grained materials,” *Materials Today*, vol. 16, no. 3. pp. 85–93, 2013.

[5] L. Y. Chen *et al.*, “Processing and properties of magnesium containing a dense uniform dispersion of nanoparticles,” *Nature*, 2015.

[6] A. R. Oganov, C. J. Pickard, Q. Zhu, and R. J. Needs, “Structure prediction drives materials discovery,” *Nature Reviews Materials*. 2019.

[7] Z. Hu, Z. Wu, C. Han, J. He, Z. Ni, and W. Chen, “Two-dimensional transition metal dichalcogenides: Interface and defect engineering,” *Chemical Society Reviews*, vol. 47, no. 9. pp. 3100–3128, 2018.

[8] I. J. Beyerlein, M. J. Demkowicz, A. Misra, and B. P. Uberuaga, “Defect-interface interactions,” *Progress in Materials Science*, vol. 74. pp. 125–210, 2015.

[9] M. Gong, J. P. Hirth, Y. Liu, Y. Shen, and J. Wang, “Interface structures and twinning mechanisms of twins in hexagonal metals,” *Mater. Res. Lett.*, vol. 5, no. 7, pp. 449–464, 2017.

[10] X. Y. Zhang *et al.*, “Twin boundaries showing very large deviations from the twinning plane,” *Scr. Mater.*, vol. 67, no. 10, pp. 862–865, 2012.

[11] Y. Li, Z. Zhang, R. Vogt, J. M. Schoenung, and E. J. Lavernia, “Boundaries and

interfaces in ultrafine grain composites," *Acta Mater.*, 2011.

[12] B. Y. Liu *et al.*, "Twinning-like lattice reorientation without a crystallographic twinning plane," *Nat. Commun.*, vol. 5, 2014.

[13] B. P. Uberuaga, L. J. Vernon, E. Martinez, and A. F. Voter, "The relationship between grain boundary structure, defect mobility, and grain boundary sink efficiency," *Sci. Rep.*, 2015.

[14] H. Jiang and I. Szlufarska, "Small-Angle Twist Grain Boundaries as Sinks for Point Defects," *Sci. Rep.*, 2018.

[15] L. Zhang, Y. Shibuta, C. Lu, and X. Huang, "Interaction between nano-voids and migrating grain boundary by molecular dynamics simulation," *Acta Mater.*, vol. 173, pp. 206–224, 2019.

[16] J. Gubicza, *X-Ray Line Profile Analysis in Materials Science*. 2014.

[17] L. Capello, T. H. Metzger, V. Holý, M. Servidori, and A. Malachias, "Structural properties of ultra-low-energy ion-implanted silicon studied by combined X-ray scattering methods," *J. Appl. Crystallogr.*, 2006.

[18] A. M. G. Carvalho *et al.*, "X-ray powder diffraction at the XRD1 beamline at LNLS," *J. Synchrotron Radiat.*, 2016.

[19] K. Nordlund, "Diffuse x-ray scattering from 311 defects in Si," *J. Appl. Phys.*, vol. 91, no. 5, pp. 2978–2983, 2002.

[20] K. Nordlund *et al.*, "Measurement of Si 311 defect properties using x-ray scattering," *J. Appl. Phys.*, vol. 98, no. 7, 2005.

[21] J. M. Oliveira, A. Malachias, C. A. Ospina, and S. O. Ferreira, "Nondestructive monitoring of defect evolution in epitaxial CdTe thin layers grown on Si(111)," *J. Phys. Chem. C*, vol. 118, no. 4, pp. 1968–1973, 2014.

[22] R. B. Figueiredo and T. G. Langdon, "Fabricating ultrafine-grained materials through the application of severe plastic deformation: A review of developments

in Brazil," *Journal of Materials Research and Technology*. 2012.

[23] Q. Li and X. Jiao, "Exploration of equal channel angular pressing routes for efficiently achieving ultrafine microstructure in magnesium," *Mater. Sci. Eng. A*, vol. 733, pp. 179–189, 2018.

[24] R. B. Figueiredo and T. G. Langdon, "Principles of grain refinement and superplastic flow in magnesium alloys processed by ECAP," *Mater. Sci. Eng. A*, vol. 501, no. 1–2, pp. 105–114, 2009.

[25] J. Koike, "New Deformation Mechanisms in Fine-Grain Mg Alloys," *Mater. Sci. Forum*, 2009.

[26] A. Galiyev, R. Kaibyshev, and G. Gottstein, "Correlation of plastic deformation and dynamic recrystallization in magnesium alloy ZK60," *Acta Mater.*, 2001.

[27] F. S. J. Poggiali, C. L. P. Silva, P. H. R. Pereira, R. B. Figueiredo, and P. R. Cetlin, "Determination of mechanical anisotropy of magnesium processed by ECAP," *J. Mater. Res. Technol.*, vol. 3, no. 4, pp. 331–337, 2014.

[28] I. J. Beyerlein, L. Capolungo, P. E. Marshall, R. J. McCabe, and C. N. Tome, "Statistical analyses of deformation twinning in magnesium," *Philos. Mag.*, 2010.

[29] G. Liu, R. Xin, F. Liu, and Q. Liu, "Twinning characteristic in tension of magnesium alloys and its effect on mechanical properties," *Mater. Des.*, vol. 107, pp. 503–510, 2016.

[30] R. B. Figueiredo, Z. Száraz, Z. Trojanová, P. Lukáč, and T. G. Langdon, "Significance of twinning in the anisotropic behavior of a magnesium alloy processed by equal-channel angular pressing," *Scr. Mater.*, 2010.

[31] J. Tu and S. Zhang, "On the $\{10\bar{1}2\}$ twinning growth mechanism in hexagonal close-packed metals," *Mater. Des.*, 2016.

[32] P. G. Partridge, "The crystallography and deformation modes of hexagonal close-packed metals," *Metall. Rev.*, vol. 12, no. 1, pp. 169–194, 2014.

[33] L. Balogh, R. B. Figueiredo, T. Ungár, and T. G. Langdon, “The contributions of grain size, dislocation density and twinning to the strength of a magnesium alloy processed by ECAP,” *Mater. Sci. Eng. A*, 2010.

[34] L. Balogh, G. Tichy, and T. Ungár, “Twinning on pyramidal planes in hexagonal close packed crystals determined along with other defects by X-ray line profile analysis,” *J. Appl. Crystallogr.*, 2009.

[35] N. Dixit, K. Y. Xie, K. J. Hemker, and K. T. Ramesh, “Microstructural evolution of pure magnesium under high strain rate loading,” *Acta Mater.*, vol. 87, pp. 56–67, 2015.

[36] S. R. Agnew and O. Duygulu, “A Mechanistic Understanding of the Formability of Magnesium: Examining the Role of Temperature on the Deformation Mechanisms,” *Mater. Sci. Forum*, 2009.

[37] M. H. Yoo, “Slip, twinning, and fracture in hexagonal close-packed metals,” *Metall. Trans. A*, 1981.

[38] J. Wang and I. J. Beyerlein, “Atomic structures of [0110] symmetric tilt grain boundaries in Hexagonal Close-Packed (hcp) crystals,” *Metall. Mater. Trans. A Phys. Metall. Mater. Sci.*, vol. 43, no. 10, pp. 3556–3569, 2012.

[39] A. Ostapovets and A. D. Sheikh-Ali, “Misorientation dependence of atomic structure and energy of symmetric tilt boundaries in magnesium,” *Philos. Mag.*, 2018.

[40] J. Als-Nielsen and D. McMorrow, *Elements of modern X-ray physics*. 2002.

[41] G. Burns, *X-Ray Diffraction*. Courier Corporation, 1985.

[42] I. R. Cole, T. R. Betts, and R. Gottschalg, “Solar profiles and spectral modeling for CPV simulations,” *IEEE J. Photovoltaics*, 2012.

[43] X. Y. Zhang *et al.*, “Twin boundaries showing very large deviations from the twinning plane,” *Scr. Mater.*, 2012.

[44] M. H. Yoo, J. R. Morris, K. M. Ho, and S. R. Agnew, “Nonbasal deformation modes of HCP metals and alloys: role of dislocation source and mobility,” *Metall. Mater. Trans. A Phys. Metall. Mater. Sci.*, vol. 33, no. 13, pp. 813–822, 2002.

[45] J. Tu, X. Y. Zhang, Y. Ren, Q. Sun, and Q. Liu, “Structural characterization of $\{101\bar{2}\}$ irregular-shaped twinning boundary in hexagonal close-packed metals,” *Mater. Charact.*, 2015.

[46] J. Megusar, “Low temperature fast-neutron and gamma irradiation of Kapton ® polyimide films,” *J. Nucl. Mater.*, 1997.

[47] M. E. Straumanis, “The precision determination of lattice constants by the powder and rotating crystal methods and applications,” *J. Appl. Phys.*, 1949.

[48] W. Kraus and G. Nolze, “POWDER CELL – a program for the representation and manipulation of crystal structures and calculation of the resulting X-ray powder patterns ,” *J. Appl. Crystallogr.*, 1996.

[49] M. Barchuk, V. Holý, D. Kriegner, J. Stangl, S. Schwaiger, and F. Scholz, “Diffuse x-ray scattering from stacking faults in a-plane GaN epitaxial layers,” *Phys. Rev. B - Condens. Matter Mater. Phys.*, vol. 84, no. 9, 2011.

[50] C. L. P. Silva, I. C. Tristão, S. Sabbaghianrad, S. A. Torbati-Sarraf, R. B. Figueiredo, and T. G. Langdon, “Microstructure and Hardness Evolution in Magnesium Processed by HPT,” *Mater. Res.*, 2017.

[51] Q. Zhu, A. Samanta, B. Li, R. E. Rudd, and T. Frolov, “Predicting phase behavior of grain boundaries with evolutionary search and machine learning,” *Nat. Commun.*, 2018.

APPENDIX

Listings are given here of MATLAB® scripts developed for the simulation routines performed in this work (I), as well as scripts that were used to generate some of the figures in this dissertation (II) and other complementary calculations (III).

MATLAB® is a registered trademark of The MathWorks, Inc. Further information can be found at *http://www.mathworks.com*.

I – Simulation Routines (MATLAB®)

A. Crystal Lattice Assembly

```
function : hcp3d_lattice(nParticles)

fmg = 12;
nPart = nParticles^2;
intRoot = floor(sqrt(nPart));
if (sqrt(nPart) - intRoot) > 1e-7
     disp('Number of particles should be a perfect square.');
     coords = zeros(2,nPart);
     Lx = 0.0;
     Ly = 0.0;
     return
end;

Q = 5.21;
sepDist = 3.2094/Q;
clatt = 5.2108;
Lx = sepDist * 1 * sqrt(nPart);
Ly = Lx*sqrt(3)/2;
Natomsc = nPart;

xPos = linspace(sepDist/2, Lx-sepDist/2, 1 * sqrt(nPart)) - Lx/2;
yPos = (sqrt(3)/2)*xPos;
[X,Y] = meshgrid(xPos,yPos);
X(1:2:end,:) = X(1:2:end,:) + sepDist/2;
maxZ = max(size(X));
Z = zeros(maxZ,maxZ) - nPart/4;
coords = [reshape(X,1,numel(X)); reshape(Y,1,numel(Y))];
X2 = X;
Y2 = Y + 0.5*sepDist;
Z2 = Z + 0.5;

natoms = numel(X);
atoms = zeros(1,1); hcpcor = zeros(1,1);
for f = 1:natoms;
    atoms(f,1) = X(f);
    atoms(f,2) = Y(f);
    atoms(f,3) = Z(f);
    atoms(f+natoms,1) = X2(f);
    atoms(f+natoms,2) = Y2(f);
    atoms(f+natoms,3) = Z2(f);
end;
for g = 2:2:(1*Natomsc)
    for f = 1:natoms;
        atoms(f+natoms*g,1) = X(f);
        atoms(f+natoms*g,2) = Y(f);
        atoms(f+natoms*g,3) = Z(f) + g*0.5;
        atoms(f+natoms*(g+1),1) = X2(f);
        atoms(f+natoms*(g+1),2) = Y2(f);
        atoms(f+natoms*(g+1),3) = Z2(f) + g*0.5;
    end;
end;

limitsphere = intRoot - 0;
maxradsphere = (sqrt(2))*(floor(limitsphere));
maxnatoms = numel(atoms(:,1));
```

```
cont = 0;
S = zeros(1,1); fmglocal = zeros(1,1); fmgreal = zeros(1,1);
for i = 1:maxnatoms
    if ((atoms(i,1)^2)+(atoms(i,2)^2)+(atoms(i,3)^2)) <= maxradsphere^2
        S(i) = 25;
        fmglocal(i) = fmg;
        cont = cont + 1;
        fmgreal(cont)= fmg;
    else
        S(i) = 1;
        fmglocal(i) = 0;
    end;
end;
atoms(:,4) = fmglocal(:);

cont = 0;
for i = 1:numel(atoms(:,4))
    if atoms(i,4) == 12
        cont = cont + 1;
        atomes(cont,:) = atoms(i,:);
    end;
end;
atomlist = atomes;
save 'mgcrystal_perf.mat' fmg sepDist clatt atomlist;
end;
```

B. Generate Matrix Projections

```
function : hcp3d_projections(fmg,sepDist,clatt,atomlist)

theta1 = input('  Choose bulk orientation, in deg [(100) is 90°]= ');
thetarad1 = theta1*(pi/180);
X1 = atomlist(:,1)*cos(thetarad1) - atomlist(:,2)*sin(thetarad1);
Y1 = atomlist(:,1)*sin(thetarad1) + atomlist(:,2)*cos(thetarad1);
Z1 = atomlist(:,3); atomproj1 = [X1 Y1 Z1 atomlist(:,4)];

theta2 = input('  Choose insertion orientation, in deg [(110) is 60°]= ');
thetarad2 = theta2*(pi/180);
X2 = atomlist(:,1)*cos(thetarad2) - atomlist(:,2)*sin(thetarad2);
Y2 = atomlist(:,1)*sin(thetarad2) + atomlist(:,2)*cos(thetarad2);
Z2 = atomlist(:,3); atomproj2 = [X2 Y2 Z2 atomlist(:,4)];
save 'mgcrystal_proj.mat' fmg sepDist clatt atomproj1 atomproj2;
end;
```

C1. Progressive Assembly of Interfaces: Out-of-Plane Rotation (α)

```
function : hcp3d_progcutA(fmg,sepDist,clatt,atomproj1,atomproj2,path,coordstep)

dcutsize = 2;
for z = coordstep
    Palpha = [ -0.8002 -6.171e-16 0 ; -0.2667 -0.308 z ; 0.8002 -0.308 z ];
    D = det(P);
    A = P; A(:,1) = 1; dA = det(A);
    B = P; B(:,2) = 1; dB = det(B);
    C = P; C(:,3) = 1; dC = det(C);
    d = 1;
    a = ((-1)*d/D)*dA;
    b = ((-1)*d/D)*dB;
    c = ((-1)*d/D)*dC;

    normP = [a b c];
    modP = sqrt((a^2)+(b^2)+(c^2));
    angle = acos(c/modP);
    theta = (pi/2)-(angle); inclangle = -theta*(180/pi);

for dp = 1:numel(atomproj1(:,1))
    distcut = abs(a*atomproj1(dp,1)+b*atomproj1(dp,2)+c*atomproj1(dp,3)+d)/sqrt(a^2+b^2+c^2);
    if distcut > dcutsize
        atomproj1(dp,4) = 12;
    else
        atomproj1(dp,4) = 0;
    end;
end;

cutatomlist = [];
cont = 0;
for i = 1:numel(atomproj1(:,4))
```

```
    if atomproj1(i,4) == 12
        cont = cont + 1;
        cutatomlist(cont,:) = atomproj1(i,:);
    end;
end;
atomcut1 = cutatomlist;

inclanglerad = (-inclangle)*(pi/180);
X = atomproj2(:,1);
Y = atomproj2(:,2)*cos(inclanglerad) - atomproj2(:,3)*sin(inclanglerad);
Z = atomproj2(:,3)*cos(inclanglerad) + atomproj2(:,2)*sin(inclanglerad);
atomproj2 = [X Y Z atomproj2(:,4)];

for dp = 1:numel(atomproj2(:,1))
    distcut = abs(a*atomproj2(dp,1)+b*atomproj2(dp,2)+c*atomproj2(dp,3)+d)/sqrt(a^2+b^2+c^2);
    if distcut < dcutsize
        atomproj2(dp,4) = 12;
    else
        atomproj2(dp,4) = 0;
    end;
end;

cutatomlist = [];
cont = 0;
for i = 1:numel(atomproj2(:,4))
    if atomproj2(i,4) == 12
        cont = cont + 1;
        cutatomlist(cont,:) = atomproj2(i,:);
    end;
end;
atomcut2 = cutatomlist;

atomdefect = [atomcut1 ; atomcut2];

save 'mgcrystal_pov.mat' atomcut1 atomcut2;
save 'mgcrystal_defect.mat' atomdefect;

atomcalc = atomdefect; atomname = 'atomdefect';
hcp3d_fft(fmg,sepDist,clatt,inclangle,atomname,atomcalc,path,coordstep);
end;
```

C2. Progressive Assembly of Interfaces: Out-of-Plane Rotation (β)

```
function : hcp3d_progcutB(fmg,sepDist,clatt,atomproj1,atomproj2,path,coordstep)

dcutsize = 2;
for z = coordstep
    Pbeta = [ -0.308 0.8002 0 ;  0.308 -0.2667 0 ; 0.308 0 z ];
    D = det(P);
    A = P; A(:,1) = 1; dA = det(A);
    B = P; B(:,2) = 1; dB = det(B);
    C = P; C(:,3) = 1; dC = det(C);
    d = 1;
    a = ((-1)*d/D)*dA;
    b = ((-1)*d/D)*dB;
    c = ((-1)*d/D)*dC;

    normP = [a b c];
    modP = sqrt((a^2)+(b^2)+(c^2));
    angle = acos(c/modP);
    theta = (pi/2)-(angle); inclangle = -theta*(180/pi);

for dp = 1:numel(atomproj1(:,1))
    distcut = abs(a*atomproj1(dp,1)+b*atomproj1(dp,2)+c*atomproj1(dp,3)+d)/sqrt(a^2+b^2+c^2);
    if distcut > dcutsize
        atomproj1(dp,4) = 12;
    else
        atomproj1(dp,4) = 0;
    end;
end;

cutatomlist = [];
cont = 0;
for i = 1:numel(atomproj1(:,4))
    if atomproj1(i,4) == 12
        cont = cont + 1;
        cutatomlist(cont,:) = atomproj1(i,:);
    end;
end;
```

```
atomcut1 = cutatomlist;

ang1 = (-30)*(pi/180);
X = atomproj2(:,1)*cos(ang1) - atomproj2(:,2)*sin(ang1);
Y = atomproj2(:,2)*cos(ang1) + atomproj2(:,1)*sin(ang1);
Z = atomproj2(:,3);
atomproj2 = [X Y Z atomproj2(:,4)];

inclanglerad = (-inclangle)*(pi/180);
X = atomproj2(:,1)*cos(inclanglerad) + atomproj2(:,3)*sin(inclanglerad);
Y = atomproj2(:,2);
Z = atomproj2(:,3)*cos(inclanglerad) - atomproj2(:,1)*sin(inclanglerad);
atomproj2 = [X Y Z atomproj2(:,4)];

ang2 = (30)*(pi/180);
X = atomproj2(:,1)*cos(ang2) - atomproj2(:,2)*sin(ang2);
Y = atomproj2(:,2)*cos(ang2) + atomproj2(:,1)*sin(ang2);
Z = atomproj2(:,3);
atomproj2 = [X Y Z atomproj2(:,4)];

for dp = 1:numel(atomproj2(:,1))
    distcut = abs(a*atomproj2(dp,1)+b*atomproj2(dp,2)+c*atomproj2(dp,3)+d)/sqrt(a^2+b^2+c^2);
    if distcut < dcutsize
        atomproj2(dp,4) = 12;
    else
        atomproj2(dp,4) = 0;
    end;
end;

cutatomlist = [];
cont = 0;
for i = 1:numel(atomproj2(:,4))
    if atomproj2(i,4) == 12
        cont = cont + 1;
        cutatomlist(cont,:) = atomproj2(i,:);
    end;
end;
atomcut2 = cutatomlist;

atomdefect = [atomcut1 ; atomcut2];

save 'mgcrystal_pov.mat' atomcut1 atomcut2;
save 'mgcrystal_defect.mat' atomdefect;

atomcalc = atomdefect; atomname = 'atomdefect';
hcp3d_fft(fmg,sepDist,clatt,inclangle,atomname,atomcalc,path,coordstep);
end;
```

C3. Progressive Assembly of Interfaces: In-Plane Rotation (γ)

```
function : hcp3d_progcutX(fmg,sepDist,clatt,atomproj1,atomproj2,path,coordstep)

dcutsize = 1;
for x = coordstep
    P = [ -0.308 0.8002 16 ; -0.308 0.8002 15 ; x -0.2667 16 ];
    D = det(P);
    A = P; A(:,1) = 1; dA = det(A);
    B = P; B(:,2) = 1; dB = det(B);
    C = P; C(:,3) = 1; dC = det(C);
    d = 1;
    a = ((-1)*d/D)*dA;
    b = ((-1)*d/D)*dB;
    c = ((-1)*d/D)*dC;

    normP = [a b c];
    modP = sqrt((a^2)+(b^2)+(c^2));
    angle = acos(a/modP);
    theta = (pi/2)-(angle); inclangle = -theta*(180/pi);

for dp = 1:numel(atomproj1(:,1))
    distcut = abs(a*atomproj1(dp,1)+b*atomproj1(dp,2)+c*atomproj1(dp,3)+d)/sqrt(a^2+b^2+c^2);
    if distcut > dcutsize
        atomproj1(dp,4) = 12;
    else
        atomproj1(dp,4) = 0;
    end;
end;

cutatomlist = []; cont = 0;
```

```
for i = 1:numel(atomproj1(:,4))
    if atomproj1(i,4) == 12
        cont = cont + 1;
        cutatomlist(cont,:) = atomproj1(i,:);
    end;
end;
atomcut1 = cutatomlist;

inclanglerad = (-inclangle)*(pi/180);
X = atomproj2(:,1)*cos(inclanglerad) - atomproj2(:,2)*sin(inclanglerad);
Y = atomproj2(:,2)*cos(inclanglerad) + atomproj2(:,1)*sin(inclanglerad);
Z = atomproj2(:,3);
atomproj2 = [X Y Z atomproj2(:,4)];

for dp = 1:numel(atomproj2(:,1))
    distcut = abs(a*atomproj2(dp,1)+b*atomproj2(dp,2)+c*atomproj2(dp,3)+d)/sqrt(a^2+b^2+c^2);
    if distcut < dcutsize
        atomproj2(dp,4) = 12;
    else
        atomproj2(dp,4) = 0;
    end;
end;

cutatomlist = [];
cont = 0;
for i = 1:numel(atomproj2(:,4))
    if atomproj2(i,4) == 12
        cont = cont + 1;
        cutatomlist(cont,:) = atomproj2(i,:);
    end;
end;
atomcut2 = cutatomlist;

atomdefect = [atomcut1 ; atomcut2];
save 'mgcrystal_pov.mat' atomcut1 atomcut2;
save 'mgcrystal_defect.mat' atomdefect;

atomcalc = atomdefect; atomname = 'atomdefect';
hcp3d_fft(fmg,sepDist,clatt,inclangle,atomname,atomcalc,path,coordstep);
end;
```

D1. Fast-Fourier Transform of Assembled Lattice: Out-of-Plane Rotations (α, β)

```
function : hcp3d_fft(fmg,sepDist,clatt,inclangle,atomname,atomcalc,path,coordstep)

path2 = strcat('angle_',num2str(inclangle),'_step_',num2str(coordstep));
mkdir(path,path2);

lambda = 1.03293;
sigma = 2.0;
lmax = 5;
Imin = 0.000;
Imax = 9.000;
Ncont = 1500;
Istep = (Imax-Imin)/Ncont;
Imin = Imin+Istep;
Imax = Imax+Istep;

atomfourier = zeros(1,Ncont+1);
Q = zeros(1,Ncont+1);
tth = zeros(1,Ncont+1);
mgfourier = zeros(Ncont+1,2);
maxnatoms = numel(atomcalc(:,1));

for hLoc = 0:3
    for kLoc = 0:1
        contloc = 1;
        for j = Imin:Istep:Imax
            lLoc = j;
            atomtemp = zeros(maxnatoms,1);
            atomsoma = 0;
            Dhkl = sqrt((3*(sepDist^2)*(clatt^2))/((4*(hLoc^2+(hLoc*kLoc)+kLoc^2))+(3*(sepDist^2)*(lLoc^2))));
            Qloc = (2*pi)/Dhkl;
            for f = 1:maxnatoms
                if atomcalc(f,4) == fmg
                    fmgLocal = 12.22064*exp(-Qloc/6.94162) + 0.09719;
                else
                    fmgLocal = 0;
                end;
```

```
                atomtemp(f,1)=(fmgLocal*exp(sigma)*(exp(2*pi*1i*(hLoc*atomcalc(f,1)+kLoc*atomcalc(f,2)+lLoc*atomcalc(f,3)))));
                atomsoma = atomsoma + atomtemp(f);
            end;
            atomfourier(contloc) = abs(atomsoma)^2;
            if atomfourier(contloc) < 0
                atomfourier(contloc) = 0;
            end;
            Q(contloc) = Qloc;
            tth(contloc) = (2*asin(Qloc*lambda/(4*pi)))*(180/pi);
            contloc = contloc + 1;
        end;
        mgfourier(:,1) = real(transpose(tth));
        mgfourier(:,2) = real(transpose(atomfourier));

        fftname = strcat(atomname,'_ang',num2str(inclangle),'_',num2str(hLoc),num2str(kLoc),'j','.txt');
        fftfile = fullfile(path,path2,fftname);
        save(fftfile,'mgfourier','-ascii');
        end;
    end;
end;
```

D2. Fast-Fourier Transform of Assembled Lattice: In-Plane Rotation (γ)

```
function : hcp3d_fftXh(fmg,sepDist,clatt,inclangle,atomname,atomcalc,path,coordstep);

path2 = strcat('angle_',num2str(inclangle),'_step_',num2str(coordstep));
mkdir(path,path2);

lambda = 1.03293;
sigma = 2.0;
lmax = 5;
Imin = 0.000;
Imax = 9.000;
Ncont = 1500;
Istep = (Imax-Imin)/Ncont;
Imin = Imin+Istep;
Imax = Imax+Istep;

atomfourier = zeros(1,Ncont+1);
Q = zeros(1,Ncont+1);
tth = zeros(1,Ncont+1);
mgfourier = zeros(Ncont+1,2);
maxnatoms = numel(atomcalc(:,1));

for kLoc = 0
    for lLoc = 0:6
        contloc = 1;
        for j = Imin:Istep:Imax
            hLoc = j;
            atomtemp = zeros(maxnatoms,1);
            atomsoma = 0;
            Dhkl = sqrt((3*(sepDist^2)*(clatt^2))/((4*(hLoc^2+(hLoc*kLoc)+kLoc^2))+(3*(sepDist^2)*(lLoc^2))));
            Qloc = (2*pi)/Dhkl;
            for f = 1:maxnatoms
                if atomcalc(f,4) == fmg
                    fmgLocal = 12.22064*exp(-Qloc/6.94162) + 0.09719;
                else
                    fmgLocal = 0;
                end;
                atomtemp(f,1)=(fmgLocal*exp(sigma)*(exp(2*pi*1i*(hLoc*atomcalc(f,1)+kLoc*atomcalc(f,2)+lLoc*atomcalc(f,3)))));
                atomsoma = atomsoma + atomtemp(f);
            end;
            atomfourier(contloc) = abs(atomsoma)^2;
            if atomfourier(contloc) < 0
                atomfourier(contloc) = 0;
            end;
            Q(contloc) = Qloc;
            tth(contloc) = (2*asin(Qloc*lambda/(4*pi)))*(180/pi);
            contloc = contloc + 1;
        end;
        mgfourier(:,1) = real(transpose(tth));
        mgfourier(:,2) = real(transpose(atomfourier));

        fftname = strcat(atomname,'_ang',num2str(inclangle),'_j',num2str(kLoc),num2str(lLoc),'.txt');
        fftfile = fullfile(path,path2,fftname);
        save(fftfile,'mgfourier','-ascii');
        end;
    end;
end;
```

```
function : hcp3d_fftXk(fmg,sepDist,clatt,inclangle,atomname,atomcalc,path,coordstep)

path2 = strcat('angle_',num2str(inclangle),'_step_',num2str(coordstep));
mkdir(path,path2);

lambda = 1.03293;
sigma = 2.0;
lmax = 5;
Imin = 0.000;
Imax = 9.000;
Ncont = 1500;
Istep = (Imax-Imin)/Ncont;
Imin = Imin+Istep;
Imax = Imax+Istep;

atomfourier = zeros(1,Ncont+1);
Q = zeros(1,Ncont+1);
tth = zeros(1,Ncont+1);
mgfourier = zeros(Ncont+1,2);
maxnatoms = numel(atomcalc(:,1));

for hLoc = 0:3
    for lLoc = 0:6
        contloc = 1;
        for j = Imin:Istep:Imax
            hLoc = j;
            atomtemp = zeros(maxnatoms,1);
            atomsoma = 0;
            Dhkl = sqrt((3*(sepDist^2)*(clatt^2))/((4*(hLoc^2+(hLoc*kLoc)+kLoc^2))+(3*(sepDist^2)*(lLoc^2))));
            Qloc = (2*pi)/Dhkl;
            for f = 1:maxnatoms
                if atomcalc(f,4) == fmg
                    fmgLocal = 12.22064*exp(-Qloc/6.94162) + 0.09719;
                else
                    fmgLocal = 0;
                end;
                atomtemp(f,1)=(fmgLocal*exp(sigma)*(exp(2*pi*1i*(hLoc*atomcalc(f,1)+kLoc*atomcalc(f,2)+lLoc*atomcalc(f,3)))));
                atomsoma = atomsoma + atomtemp(f);
            end;
            atomfourier(contloc) = abs(atomsoma)^2;
            if atomfourier(contloc) < 0
                atomfourier(contloc) = 0;
            end;
            Q(contloc) = Qloc;
            tth(contloc) = (2*asin(Qloc*lambda/(4*pi)))*(180/pi);
            contloc = contloc + 1;
        end;
        mgfourier(:,1) = real(transpose(tth));
        mgfourier(:,2) = real(transpose(atomfourier));

        fftname = strcat(atomname,'_ang',num2str(inclangle),'_',num2str(hLoc),'j',num2str(lLoc),'.txt');
        fftfile = fullfile(path,path2,fftname);
        save(fftfile,'mgfourier','-ascii');
        end;
    end;
end;
```

```
function : hcp3d_fftXhk(fmg,sepDist,clatt,inclangle,atomname,atomcalc,path,coordstep)

path2 = strcat('angle_',num2str(inclangle),'_step_',num2str(coordstep));
mkdir(path,path2);

lambda = 1.03293;
sigma = 2.0;
lmax = 5;
Imin = 0.000;
Imax = 9.000;
Ncont = 1500;
Istep = (Imax-Imin)/Ncont;
Imin = Imin+Istep;
Imax = Imax+Istep;

atomfourier = zeros(1,Ncont+1);
Q = zeros(1,Ncont+1);
tth = zeros(1,Ncont+1);
mgfourier = zeros(Ncont+1,2);
maxnatoms = numel(atomcalc(:,1));
```

```

for lLoc = 0:6
    for hLoc = Imin:Istep:Imax
        contloc = 1;
        for j = Imin:Istep:Imax
            lLoc = j;
            atomtemp = zeros(maxnatoms,1);
            atomsoma = 0;
            Dhkl = sqrt((3*(sepDist^2)*(clatt^2))/((4*(hLoc^2+(hLoc*kLoc)+kLoc^2))+(3*(sepDist^2)*(lLoc^2))));
            Qloc = (2*pi)/Dhkl;
            for f = 1:maxnatoms
                if atomcalc(f,4) == fmg
                    fmgLocal = 12.22064*exp(-Qloc/6.94162) + 0.09719;
                else
                    fmgLocal = 0;
                end;
                atomtemp(f,1)=(fmgLocal*exp(sigma)*(exp(2*pi*1i*(hLoc*atomcalc(f,1)+kLoc*atomcalc(f,2)+lLoc*atomcalc(f,3)))));
                atomsoma = atomsoma + atomtemp(f);
            end;
            atomfourier(contloc) = abs(atomsoma)^2;
            if atomfourier(contloc) < 0
                atomfourier(contloc) = 0;
            end;
            Q(contloc) = Qloc;
            tth(contloc) = (2*asin(Qloc*lambda/(4*pi)))*(180/pi);
            contloc = contloc + 1;
        end;
        mgfourier(:,1) = real(transpose(tth));
        mgfourier(:,2) = real(transpose(atomfourier));

        fftname = strcat(atomname,'_ang',num2str(inclangle),'_',num2str(hLoc),num2str(kLoc),'j','.txt');
        fftfile = fullfile(path,path2,fftname);
        save(fftfile,'mgfourier','-ascii');
        end;
    end;
end;
```

E. Executable

```
clear;
path = strcat('C:/Users/USER/Desktop/hcp3d_plots/',datestr(clock,'dd-mmm-yyyy HH.MM.SS')); mkdir(path);
disp(datestr(clock,'dd-mmm-yyyy HH.MM.SS'));

fprintf('\n'); disp('- HCP LATTICE -'); disp('Define the crystal lattice size.');
nParticles = input('  nPart = ');
fprintf('  wait ...\n');
hcp3d_lattice(nParticles);
load mgcrystal_perf.mat;

fprintf('Enter information on plane projections.\n');
hcp3d_projections(fmg,sepDist,clatt,atomlist);
load mgcrystal_proj.mat;

planestep = input('Choose between alpha/beta or gamma [z/x]: ','s');
if planestep == 'z'
    for step = %insert manually%
        if step == 0
            step = -1e-007;
        end;
        coordstep = step;
        hcp3d_progcut(fmg,sepDist,clatt,atomproj1,atomproj2,path,coordstep);
    end;
    fprintf('- END - Total elapsed time is %g seconds.\n',time);
elseif planestep == 'x'
    for step = %insert manually%
        coordstep = step;
        hcp3d_progcutX(fmg,sepDist,clatt,atomproj1,atomproj2,path,coordstep);
    end;
    fprintf('- END - Total elapsed time is %g seconds.\n',time);
else
    disp('Please return a valid input! Try again.');
    break;
end;
disp('_____________________________________________________________________');
```

II – Extraction of Atom Matrices Figures for POV-Ray™ (MATLAB®)

A. Extraction of Bulk Matrix (Full Bulk + Projections)

```
load mgcrystal_proj.mat;
path = strcat('C:/Users/USER/Desktop/hcp3d_plots/POV-Ray/bulk - ',datestr(clock,'dd-mmm-yyyy HH.MM.SS')); mkdir(path);

%% ATOMLIST
atompov = [];
cont = 0;
for i = 1:numel(atomlist(:,3))
    if atomlist(i,3) >= -5
        if atomlist(i,3) <= 5
            if atomlist(i,1) >= -1
                if atomlist(i,1) <= 1
                    cont = cont + 1;
                    atompov(cont,1) = atomlist(i,1);
                    atompov(cont,2) = atomlist(i,2);
                    atompov(cont,3) = atomlist(i,3);
                end;
            end;
        end;
    end;
end;

for j = 1:numel(atompov(:,3))
    if abs(atompov(j,1)) < 0.0000001
        atompov(j,1) = 0.00000;
    end;
end;
for j = 1:numel(atompov(:,3))
    if abs(atompov(j,2)) < 0.0000001
        atompov(j,2) = 0.00000;
    end;
end;

arq = strcat(path,'/atomlist.pov');
lines = [];
for line = 1:numel(atompov(:,1));
    povstr=strcat('sphere{<',num2str(atompov(line,1)),',',num2str(atompov(line,2)),',',num2str(atompov(line,3)),'>,0.13}');
    lines = strvcat(lines,povstr);
    disp(line)
end;
dlmwrite(arq,lines,'');

%% ATOMPROJ1
atompov = [];
cont = 0;
for i = 1:numel(atomproj1(:,3))
    if atomproj1(i,3) >= -5
        if atomproj1(i,3) <= 5
            if atomproj1(i,1) >= -1
                if atomproj1(i,1) <= 1
                    cont = cont + 1;
                    atompov(cont,1) = atomproj1(i,1);
                    atompov(cont,2) = atomproj1(i,2);
                    atompov(cont,3) = atomproj1(i,3);
                end;
            end;
        end;
    end;
end;

for j = 1:numel(atompov(:,3))
    if abs(atompov(j,1)) < 0.0000001
        atompov(j,1) = 0.00000;
    end;
end;
for j = 1:numel(atompov(:,3))
    if abs(atompov(j,2)) < 0.0000001
        atompov(j,2) = 0.00000;
    end;
end;

arq = strcat(path,'/atomproj1.pov');
lines = [];
for line = 1:numel(atompov(:,1));
    povstr=strcat('sphere{<',num2str(atompov(line,1)),',',num2str(atompov(line,2)),',',num2str(atompov(line,3)),'>,0.13}');
    lines = strvcat(lines,povstr);
```

```
    disp(line)
end;
dlmwrite(arq,lines,'');

%% ATOMPROJ2
atompov = [];
cont = 0;
for i = 1:numel(atomproj2(:,3))
    if atomproj2(i,3) >= -5
        if atomproj2(i,3) <= 5
            if atomproj2(i,1) >= -1
                if atomproj2(i,1) <= 1
                    cont = cont + 1;
                    atompov(cont,1) = atomproj2(i,1);
                    atompov(cont,2) = atomproj2(i,2);
                    atompov(cont,3) = atomproj2(i,3);
                end;
            end;
        end;
    end;
end;

for j = 1:numel(atompov(:,3))
    if abs(atompov(j,1)) < 0.0000001
        atompov(j,1) = 0.00000;
    end;
end;
for j = 1:numel(atompov(:,3))
    if abs(atompov(j,2)) < 0.0000001
        atompov(j,2) = 0.00000;
    end;
end;

arq = strcat(path,'/atomproj2.pov');
lines = [];
for line = 1:numel(atompov(:,1));
    povstr=strcat('sphere{<',num2str(atompov(line,1)),',',num2str(atompov(line,2)),',',num2str(atompov(line,3)),'>,0.13}');
    lines = strvcat(lines,povstr);
    disp(line)
end;
dlmwrite(arq,lines,'');
```

III – Data Retrieval (MATLAB®)

A. Maximum Estimated Strain (1D Distortion)

```
clear;
lambda = 1.03293;
tthsim = %insert manually%
tthexp = %insert manually%

distexp = lambda/(2*sin((tthexp*(pi/180))/2));
distsim = lambda/(2*sin((tthsim*(pi/180))/2));
str = ((distexp-distsim)/distsim)*100;

fprintf('- Strain - \nfor tthsim = %g° \n    str = %g \n\n',tthsim,str);
```

B. Miller Index Estimate (*l* only)

```
clear;
lambda = 1.03293;
sepDist = 3.2094; clatt = 5.2108;

hLoc = %insert manually%
kLoc = %insert manually%
tthsim = %insert manually%

tthrad = tthsim*(pi/180);
lLoc = sqrt((4*(clatt^2))*(((sin(tthrad/2)^2)/(lambda^2))-((hLoc^2 + (hLoc*kLoc) + kLoc^2)/(sepDist^2))/3));
fprintf('for tthsim = %g° \n    lLoc = %g \n\n',tthsim,lLoc);
```